PI-(3,5)P2-mediated oligomerization of the endosomal sodium/proton exchanger NHE9

Surabhi Kokane[1*], Pascal F. Meier[1*], Ashutosh Gulati[1*], Rei Matsuoka[1*], Tanadet Pipatpolkai[2], Giuseppe Albano[3], Lucie Delemotte[2], Daniel Fuster[3], David Drew[1#]

[1]Department of Biochemistry and Biophysics, Science for Life laboratory, Stockholm University, SE-106 91 Stockholm, Sweden. [2]Department of Applied Physics, Science for Life Laboratory, KTH Royal Institute of Technology, Stockholm, Sweden. [3]Department of Nephrology and Hypertension, Inselspital, Bern University Hospital and University of Bern, Bern, Switzerland

*These authors contributed equally

#Correspondence: ddrew@dbb.su.se

Abstract

Na^+/H^+ exchangers are found in all cells to regulate intracellular pH, sodium levels and cell volume. Na^+/H^+ exchangers are physiological homodimers that operate by an elevator alternating-access mechanism. While the structure of the core ion translocation domain is fairly conserved, the scaffold domain and oligomerization show larger structural variation. The Na^+/H^+ exchanger NhaA from *E. coli* has a weak oligomerization interface mediated by a β-hairpin domain and homodimerization was shown to be dependent of the lipid cardiolipin. Organellar Na^+/H^+ exchangers NHE6, NHE7 and NHE9 are likewise predicted to contain β-hairpin domains and a recent analysis of *horse* NHE9 indicated that the lipid PIP_2 binds at the dimerization interface. Despite predicted lipid-mediated oligomerization, their structural validation has been lacking. Here, we report cryo-EM structures of *E. coli* NhaA and *horse* NHE9 with the coordination of cardiolipin and $PI(3,5)P_2$ binding at the dimer interface, respectively. Cell based assays confirms that NHE9 is inactive at the plasma membrane and thermal-shift assays, solid-supported membrane (SSM) electrophysiology and MD simulations, corroborates that NHE9 specifically binds the endosomal $PI(3,5)P_2$ lipid, which stabilizes the homodimer and enhances activity. Taken together, we propose specific lipids regulate Na^+/H^+ exchange activity by stabilizing oligomerization and stimulating Na^+ binding under lipid-specific cues.

Introduction

Na^+/H^+ exchangers facilitate the exchange of cations ($Na^+/Li^+/K^+$) and protons (H^+) across membranes to regulate intracellular pH, sodium levels and cell volume (Pedersen & Counillon, 2019). In bacteria these ancient proteins work to either generate a sodium-motive-force or to alleviate sodium-salt stress (Krulwich *et al*, 2011; Padan, 2008). In mammals, there are 13 different Na^+/H^+ exchangers (NHE) belonging to the SLC9A (NHE1-9), SLC9B (NHA1-2) or sperm specific SLC9C families (Fuster & Alexander, 2014; Pedersen & Counillon, 2019). NHEs differ in their substrate preferences, kinetics, subcellular and tissue distribution (Pedersen & Counillon, 2019). Isoforms NHE1-5 are primarily expressed on the plasma membrane and have important physiological roles linked to cellular pH homeostasis (Pedersen & Counillon, 2019). Isoforms NHE6-9 are primary localized to intracellular compartments and work in concert with the V-type ATPase to fine-tune pH in their respective organelles.

Na^+/H^+ exchangers are physiological homodimers belonging to the "NhaA-fold", so-named after the first fold-representative to be determined (Brett *et al*, 2005; Fliegel, 2019; Padan, 2008). The transporter is made up of two distinct domains, a dimerization domain and an ion-transporting (core) domain. The 6-TM core domain undergoes global, elevator-like structural transitions to translocate ions across the membrane against the anchored dimerization domain (Coincon *et al*, 2016; Drew & Boudker, 2016). The cryo-EM structures of SLC9A, SLC9B and SLC9C have been determined and show a similar architecture to bacterial homologue structures with 13 transmembrane (TM) helices (Hunte *et al*, 2005a; Lee *et al*, 2013; Matsuoka *et al*, 2022; Paulino *et al*, 2014; Wohlert *et al*, 2014; Yeo *et al*, 2023). Folds of secondary-active transporters are nearly always made up from a conserved repeat unit that is related by internal structural-symmetry (Forrest, 2015). Interestingly, the structural-inverted repeats in proteins with the NhaA-fold seem to be the only transporter members where the structural-repeat unit varies between members. NhaA is made up of 12 TMs and has a 5-TM structural-inverted repeat, SLC9A and SLC9C are made up of 13-TMs and have a 6-TM repeat, whereas SLC9B has 14-TMs and a 7-TM repeat (Matsuoka *et al.*, 2022; Yeo *et al.*, 2023). Although the 6-TM core domain of NhaA that translocates the ions across the membrane is conserved, the additional number of helices alters the structure of the dimerization interface. It seems that there has been evolutionary pressure to fine-tune oligomerization in the NhaA-fold for a functional reason.

78 Previous studies using native MS, MD simulations and thermal-shift assays, identified
79 that NhaA oligomerization is dependent on cardiolipin (Gupta *et al*, 2017; Nji *et al*,
80 2018; Rimon *et al*, 2019; Winkelmann *et al*, 2022). NhaA has a weak dimer interface
81 mediated by a β-hairpin domain, which may make dimerization and activity more lipid-
82 dependent than of other Na^+/H^+ exchangers. Consistent with this reasoning,
83 dimerization in other bacterial Na^+/H^+ exchangers lacking β-hairpins and with a larger
84 dimerization interface, were found to be lipid-independent (Gupta *et al.*, 2017). It was
85 further shown that NhaA was unable to compensate salt-stress in a *E. coli* strain
86 deficient in cardiolipin (Rimon *et al.*, 2019). Since cardiolipin biosynthesis in *E. coli* is
87 increased upon salt-stress and, because NhaA is required to alleviate salt-stress (Padan,
88 2008; Romantsov *et al*, 2009), it was thus proposed that lipid binding might be a means
89 to regulate *in vivo* NhaA activity. Despite this attractive hypothesis, structural validation
90 of cardiolipin binding to *E. coli* NhaA has been lacking.

91 In addition to NhaA, native mass-spectrometry and thermal-shift assays have also
92 shown that the endosomal Na^+/H^+ exchanger NHE9 (SLC9A9) dimer co-purifies with
93 negatively-charged lipids matching the mass of PIP_2 (Winklemann *et al*, 2020). NHE9
94 regulates the luminal pH of late- and recycling endosomes (Kondapalli *et al*, 2015;
95 Kondapalli *et al*, 2014) and mutations in SLC9A9 have been associated with
96 neurological disorders such as familial autism, ADHD and epilepsy (Kondapalli *et al.*,
97 2014; Zhang-James *et al*, 2019). Interestingly, although endosomal NHE9 has a larger
98 dimer interface than NhaA and is similar in size to plasma membrane localised NHE1
99 (Dong *et al*, 2021) (Fig. 1A), the NHE9 protein has an additional ~ 60 residue extension
100 of the TM2 -TM3 loop, which AlphaFold 2 predicts forms a β-hairpin (Fig. 1B, C)
101 (Jumper *et al*, 2021). The TM2-TM3 loop is only present in organellar isoforms NHE6,
102 NHE7 and NHE9 (Fig. 1C) and, similar to NhaA, multimer AlphaFold2 predicts the β-
103 hairpins will interact with each other at the dimerization interface (Fig. 1D) (Jumper *et*
104 *al.*, 2021), but this region was too dynamic to be modelled in previous cryo EM
105 structures (Fig. 1E) (Winklemann *et al.*, 2020). Although, it is currently unclear if the
106 TM2-TM3 loop domain contributes to lipid binding, the mutation of two lysine residues
107 Lys105 and Lys107 in the unresolved TM2-TM3 loop domain, was sufficient to abolish
108 PIP_2 stabilization, indicating this might be the case (Winklemann *et al.*, 2020).

109 Here, we set out to determine cryo-EM structures of the β-hairpin containing NhaA and

NHE9 Na^+/H^+ exchangers to resolve the proposed lipid-mediated oligomerization and to establish how lipid-binding can allosterically regulate exchange activity.

Results

Cryo EM structure of the NhaA homodimer at pH 7.5 bound to CDL

E. coli NhaA has become a model system for Na^+/H^+ exchangers (Padan, 2008; Winkelmann *et al.*, 2022). Despite extensive biochemical, biophysical, and computational analysis, most structures of NhaA were crystallized as monomers (Hunte *et al.*, 2005a; Winkelmann *et al.*, 2022). The NhaA homodimer was been crystallized, but at 3.5 Å resolution it was unclear if lipids mediated dimerization (Lee *et al*, 2014). As such, a *Ec*NhaA WT-like triple mutant (A109T, Q277G, L296M) was purified in detergent supplemented with cardiolipin (CDL) for cryo EM studies. In brief, from optimized grids, a data-set of 14,329 movies was collected and, after processing, a cryo EM map at 3.3 Å resolution could be obtained, according to the gold-standard Fourier shell correlation (FSC) 0.143 criterion (Supplementary Fig. 1A-C, Table 1).

Similar to previous NhaA crystal structures, the cryo EM structure of NhaA adopts the inward-facing conformation (Fig. 2A) (Hunte *et al*, 2005b; Winkelmann *et al.*, 2022). Between inactive pH 4 and partially-active pH 6.5, a conformational switch termed a pH sensor/gate allows hydrated Na^+ ions to enter the cavity and controls the pH at which NhaA becomes activated (Fig. 2A) (Padan *et al*, 2004; Winkelmann *et al.*, 2022). As such, the mutation of charged residues on the cytoplasmic surface can alter the pH of NhaA activation and mutation of surface histidine residues to alanine abolished activity altogether (Padan *et al.*, 2004; Winkelmann *et al.*, 2022). Similar to the monomeric crystal structure at pH 6.5 (Winkelmann *et al.*, 2022), an intracellular cavity in the cryo EM structure at pH 7.5 has opened to enable Na^+ accessibility to the ion-binding (Fig. 2A).

The cryo EM structure of NhaA retained the physiological homodimer (Fig. 2B). As expected from native MS and MD simulations (Gupta *et al.*, 2017), thermal-shift assays (Nji *et al.*, 2018), and functional activity analysis (Quick *et al*, 2021; Rimon *et al.*, 2019) clear map density to supports the modelling of cardiolipin at the dimerization interface (Fig. 2B). One CDL was present in the middle of the positively-charged

143 dimerization interface, flanked by two additional CDL lipids bound towards the ends
144 of the dimer interface (Fig. 2C). Although this part of the dimerization interface is very
145 positively-charged with four arginine side chains per protomer contributing — Arg203,
146 Arg204, Arg245 and Arg250 — only the Arg204 residue directly interacts with the
147 phosphate headgroups of the central CDL. Additional hydrogen bonds are contributed
148 by Thr205 and Trp258 to oxygen atoms of CDL phosphoester bonds (Fig. 2D). Deeper
149 in the cleft, the side chain of Trp258 hydrogen bonds to Arg204, and also interacts with
150 both the central and the flanking CDL molecules, sandwiched between the distal
151 glycerol moieties of both the middle and the flanking CDL lipids. The flanking CDL
152 molecules hydrogen bonds to Arg204, and the backbone oxygens of Gly201, Ala202
153 and Arg203.
154
155 The co-ordination of CDL seen in *Ec*NhaA triple mutant is entirely consistent with
156 computational analysis of CDL binding sites from analysis of more than 40 different *E.*
157 *coli* proteins (Corey *et al*, 2021). Moreover, an Arg203Ala and Arg204Ala double-
158 mutant abolished thermostabilization of NhaA by CDL (Winkelmann *et al.*, 2022). The
159 ion-binding site is located between cross-over helices in the core domain, yet
160 accessibility to the ion-binding site is likely to be influenced by hydrophobic gating
161 residues on the dimerization helix of TM2 (Matsuoka *et al.*, 2022; Okazaki *et al*, 2019).
162 It seems that stabilization of the scaffold by CDL might favour Na^+ accessibility to the
163 ion-binding site, which would be consistent with the higher affinity for $^{22}Na^+$ as
164 measured upon the addition of CDL to detergent-solubilised NhaA (Quick *et al.*, 2021).
165
166 *Cryo-EM structure of NHE9* with TM2-TM3 β-hairpin loop domain at low pH 6.5*
167 NHE9 was predicted by AlphaFold2 (Jumper *et al*, 2021) to harbour a β-hairpin loop
168 domain between the topologically equivalent helices, TM2-TM3, to the β-hairpins in
169 NhaA (Fig. 1D, Supplementary Fig. 2A). In the AlphaFold2 NHE9 monomer vs
170 multimer prediction, the β-hairpins in NHE9 re-adjust their position to interact with the
171 β-hairpin from the neighbouring protomer (Supplementary Fig. 2B). The previous
172 structure of *horse* NHE9* (residues 8 to 574; out of 645) by cryo-EM was determined
173 from protein purified in the detergents LMNG and CHS at pH 7.5, but map density was
174 too poor to model this loop domain (Fig. 1E) (Winklemann *et al.*, 2020). Here, we
175 repeated the collection of NHE9* instead at pH 6.5 where NHE9 is thought to be less

active, and therefore presumably less dynamic. Overall, we collected ~4,300 movies and the final 3D-reconstruction contained data of ~244,279 particles, from which an EM map could be reconstructed to 3.3 Å according to the gold-standard Fourier shell correlation (FSC) 0.143 criterion (Supplementary Fig. 3A). Comparison of the NHE9* structures determined at pH 7.5 and pH 6.5 showed no apparent differences (Supplementary Fig. 3B). We speculated that the respective final 3D reconstructions may still contain heterogeneity and we therefore performed 3D-variability analysis in CryoSPARC (Punjani *et al*, 2017), followed by clustering (principal component) analysis to separate further classes. Selecting 42% of the particles for heterogeneous refinement, enabled an improved cryo EM map reconstruction of NHE9* at pH 6.5, with additional map features for the TM2-TM3 loop domain (Supplementary Fig. 4). Further homogenous refinement with C2 symmetry improved the cryo EM density for the TM2-TM3 loop domain with an overall resolution estimate of 3.6 Å (Supplementary Fig. 4A), although the map resolution seems poorer at ~ 4.2 Å resolution. As a last-step, a composite map was generated for model building, combining the additional TM2-TM3 loop domain features with the higher resolution EM maps (Supplementary Fig. 4B). Subsequently, we refined the AlphaFold2 NHE9 multimer model into the NHE9* cryo-EM maps with some further manual adjustment where needed (Methods and Fig. 3A-B).

At the extracellular end of TM2, a flexible loop of residues Pro72 to Asp82, were predicted by AlphaFold2 as extending towards the centre of the dimerization interface, followed by short-linker and a β-hairpin strand angled 60° away from the NHE9* surface (Fig. 3A). We were able to confidently refine the overall position of the short linker and β-hairpin strand that fits the AlphaFold2 model (Fig. 3A). The loop domain reconnects to the beginning of TM3 *via* a short extracellular helix (ECH1), which was well supported by the cryo EM maps (Fig. 3A). The β-hairpins are predicted by AF2 to be domain-swapped, and this arrangement refines well into the map density. The centre of the loop domain has a cluster of positively-charged residues Lys105, Lys107 and Arg108 from each of the two protomers (Fig. 3A). Overall, the TM2-TM3 β-loop domain clasps the two protomers together on the luminal side, and forms a highly positively-charged cluster that is now located above the dimerization domain interface. As such, the re-modelled NHE9* structure is consistent with its previously proposed

requirement for binding negatively-charged PIP_2 lipids at the interface (Winklemann *et al.*, 2020).

*Cryo-EM structure of cysteine variant (NHE9*CC) shows binding of PI(3,5)P_2 lipids*

To improve the resolution of the NHE9* structure we substituted Leu139 and Ile444 residues to cysteines in an attempt to disulphide-trap the inward-facing state. In addition, we added brain lipids during each step of the NHE9*CC affinity purification (see Methods). We subsequently collected a larger data-set of 13,780 movies and the final 3D-reconstruction had 78,370 particles from which an EM map was reconstructed to 3.2 Å according to the gold-standard Fourier shell correlation (FSC) 0.143 criterion (Supplementary Fig. 5A). Despite the similar FSC resolution estimate, these cryo-EM maps were improved with some local regions extending to 2.5 Å resolution (Supplementary Fig. 5A). In particular, the density was clearer for the TM2-TM3 β-loop at lower contour levels (Supplementary Fig. 5A). Map density and sulphur atom distances, however, did not support disulphide bond formation between the two introduced cysteine residues (Supplementary Fig. 6A-B). Currently, it is unclear whether the improved map quality for NHE9*CC is due to the introduced cysteine mutations, or by the repeated addition of lipids during purification.

At the dimerization interface we further observe additional lipid-like features in the improved cryo EM maps (Fig. 3B and Supplementary Fig. 6C). Rather than the cylinder-like density of fatty acids seen in the NHE1 nanodisc structure in POPC lipids (Dong *et al*, 2021), the cryo-EM maps show larger, head-group lipid densities with distinct features (Fig. 3B, Supplementary Fig. 6C). Given that NHE9* co-purified from yeast with several lipids corresponding to the molecular mass of PIP_2 (Winklemann *et al.*, 2020), we attempted to model two PIP_2 molecules into the NHE9* CC maps and found that the density was a better fit for the lipid phosphatidylinositol-3,5-bisphosphate PI(3,5)$P_{2,}$, rather than predominantly found phosphatidylinositol-4,5-bisphosphate PI(4,5)P_2 lipids (Fig. 3B, Supplementary Fig. 6C) — although PI(3,5)P_2 is a minor PIP_2 lipid, it is specific to late endosomes and lysosomes, which overlaps with the functional localization of NHE9 (Hasegawa *et al*, 2017) whereas PI(4,5)P_2 is principally found at the plasma membrane (Ho *et al*, 2012). The glycerol backbone and acyl chains of the PI(3,5)P_2 lipid form hydrophobic stacking interactions to Trp321

242 (TM8, TM8') (Fig. 3C). Two glutamine residue Gln17 (TM1, TM1') and Asn136
243 (TM3, TM3') are well positioned to hydrogen-bond with the phosphomonoester in the
244 C3-OH position (Fig. 3C). The position of these polar residues could partially explain
245 the preference for PI(3,5)P_2 lipids, since there are no polar residues close enough to
246 interact with a PO_4^{2-} at the C4-OH position.

247 Masked refinement of NHE9*CC was required to obtain high resolution maps to model
248 PI(3,5)P_2 lipids, but map features for the TM2-TM3 β-hairpin loop domain could not
249 be retained, likely as its too dynamic (Supplementary Fig. 5A). Nevertheless, at lower
250 contour levels, the map density for the β-hairpin loop domain matches the map density
251 seen in the NHE9* maps at pH 6.5 (Supplementary Fig. 5A). With a rigid-body fit of
252 the TM2-TM3 β-hairpin loop domain modelled into the NHE9*CC maps, the
253 positively-charged loop domain residues Lys105, Lys105' Lys107, Lys107' could
254 neutralise the negatively-charge headgroups of PI(3,5)P_2 (Fig. 3D). Consistently,
255 mutation of these lysine residues to glutamine was previously shown to abolish PIP_2 -
256 induced thermostabilization of NHE9 (Winklemann *et al.*, 2020).

257 To evaluate if the lysine residues could interact with the modelled PIP_2 lipids as
258 expected, we carried out molecular dynamics (MD) simulations of the NHE9*CC
259 structure and a *in silico* model for an NHE9* Lys85Gln-Lys105Gln-Lys107Gln variant
260 (see Methods). In MD simulations, the PI(3,5)P_2 lipid stayed within less than 3 Å from
261 its initial position for nearly the entire simulation time (Fig. 4A,B). In contrast, a
262 modelled PI(4,5)P_2 lipid was less stably bound with a higher fraction of frames showing
263 > 3 Å movement from its initial position (Fig. 4B). The distribution of salt-bridge
264 interactions with Lys105 and Lys107 residues revealed that Lys105 residues were
265 nearly always in contact with the PI(3,5)P_2 lipid, whereas Lys107 residues remained in
266 contact for around half of the simulation time (Fig. 4C,E). The PI(4,5)P_2 lipid had a
267 much larger variation for interaction with the lysine residues and the preferred
268 interaction with Lys105 was less pronounced (Fig. 4D, E). In MD simulations of the
269 modelled NHE9* Lys85Gln-Lys105Gln-Lys107Gln variant, neither of the PIP_2 lipids
270 were stably bound and the lipids had no clear interaction with the modelled glutamines
271 (Fig. 4B-D). Overall, the MD simulations support that lysine residues in the TM2-TM3
272 β-hairpin loop can form stable interactions with the modelled PI(3,5)P_2 lipids observed
273 in the NHE9*CC variant. Thus, the polar and aromatic residues located at the

274 dimerization interface and together with positive-charged residues from the TM2-TM3
275 β-hairpin loop, create an environment well-suited for binding the endosomal specific
276 $PI(3,5)P_2$ lipid (Fig. 3D).

277 *Assessing the requirement of $PI(3,5)P_2$ lipid binding to NHE9*

278 We had previously probed interactions with PIP_2 and PIP_3 lipids to NHE9* using FSEC-
279 TS and GFP-based thermal stability assays (Hattori *et al*, 2012; Nji *et al.*, 2018;
280 Winklemann *et al.*, 2020), which we had earlier confirmed could detect cardiolipin-
281 specific stabilization of *E. coli* NhaA (Landreh *et al*, 2017; Nji *et al.*, 2018). The average
282 melting temperature (ΔT_m) of NHE9* increased by 8°C with $PI(4,5)P_2$ addition,
283 whereas other lipids POPC, POPE and POPA showed no clear thermostabilization
284 (Winklemann *et al.*, 2020). To validate that $PI(3,5)P_2$ would also stabilise NHE9* in a
285 similar manner, NHE9* GFP-TS melting curves were recorded in the presence of either
286 $PI(4,5)P_2$ or $PI(3,5)P_2$ lipids (Methods and Fig. 5A). Consistently, NHE9* displayed
287 higher thermostabilization with $PI(3,5)P_2$ addition with a ΔT_m of 15°C, as compared to
288 ΔT_m of 8°C for $PI(4,5)P_2$ addition. Without lipid addition, NHE9* unfolds around 30°C
289 with a shallow slope for the transition temperature, which is indicative of a mixed
290 protein population (Fig. 5A). In contrast, with $PI(3,5)P_2$ added, NHE9* melted with a
291 sharper transition, indicating a shift to a more uniform protein species (Fig. 5A).
292
293 In the presence of various lipids, we further assessed the relationship between resistance
294 to heat denaturation and retention of the NHE9 homodimer by FSEC (Methods). As
295 anticipated, we observed that a higher fraction of the NHE9* homodimer was retained
296 if $PI(3,5)P_2$ lipid was added prior to heating (50ºC for 10 mins), versus either $PI(4,5)P_2$
297 or POPC lipid addition (Fig. 5B). We had previously shown that substitution of β-
298 hairpin TM2-TM3 lysine residues to glutamine in NHE9* Lys85Gln-Lys105Gln-
299 Lys107Gln abolished $PI(4,5)P_2$ stabilization and oligomerization using native MS
300 (Winklemann *et al.*, 2020). Consistently, the NHE9* Lys85Gln-Lys105Gln-Lys107Gln
301 variant purified as a monomer in detergent, and the addition of either $PI(3,5)P_2$,
302 $PI(4,5)P_2$ or POPC lipids showed no clear thermostabilization (Supplementary Fig.
303 7A,B). Taken together, thermostability-shift assays confirms that NHE9* binds lipid
304 $PI(3,5)P_2$ and its addition stabilises the functional homodimer in detergent.
305
306

307 NHE9 is localized to endosomes (Nakamura *et al*, 2005). If PI(3,5)P2 lipids are
308 required for NHE9 activity, then the protein might be inactive in membranes lacking
309 this lipid. To assess the requirement of NHE9 activity for endosomal-specific lipids, we
310 expressed *human* NHE9 and plasma membrane localized *human* NHE1 in a PS120 cell
311 line, which is deficient in plasma membrane NHEs (Methods). In this mutant cell line,
312 plasma membrane localization of both *human* NHE1 and NHE9 isoform was confirmed
313 after their transient transfection by surface biotinylation, isolation and
314 immunoprecipitation (Fig. 5C). To measure *human* NHE1 and NHE9 activity, the pH-
315 sensitive dye BCECF was trapped intracellularly and pH recovery after acid loading
316 with NH_4Cl assessed spectroscopically. Whilst sodium-dependent intracellular pH
317 recovery was clearly measurable in PS120 cells expressing *human* NHE1, no NHE
318 activity could be measured for *human* NHE9, despite similar expression levels (Fig. 5C
319 and D). Thus, we can confirm that *human* NHE9 is inactive when mistargeted to the
320 plasma membrane.

321 As it is practically infeasible to incorporate PI(3,5)P_2 lipids into the plasma membrane
322 of cultured cells, we required another approach to assess whether NHE9 activity is also
323 dependent on PIP_2 lipids. Previously, NHE9* was reconstituted into liposomes together
324 with F_0F_1-ATP synthase for proteoliposome studies and an apparent K_M of NHE9* for
325 Na^+ of 20.5 ± 3 mM was determined (Winklemann *et al.*, 2020). However, a high
326 background from empty liposomes would make assessing lipid requirements for
327 NHE9* challenging in this set-up, as the signal-to-noise ratio was previously low ~ 3:1
328 and the bacterial ATPase protein has different lipid preferences to NHE9. More recently,
329 we have used solid-supported membrane (SSM) electrophysiology to record Na^+
330 translocation of SLC9B2 and SLC9C1 Na^+/H^+ exchangers (Matsuoka *et al.*, 2022; Yeo
331 *et al.*, 2023). In this setup, proteoliposomes containing NHEs are adsorbed to a SSM
332 and charge translocation is measured *via* capacitive coupling of the supporting
333 membrane, following accumulation of transported ions (Bazzone *et al*, 2017).

334 We forthwith recorded SSM responses for NHE9* proteoliposomes upon the addition
335 of 20 mM NaCl (Supplementary Fig. 7C and Methods). Peak currents were ~6-fold
336 higher than either the NHE9* variant for which ion-binding site residues Asn243 and
337 Asp244 were substituted to alanine, or the unrelated mammalian transporter for fructose
338 (GLUT5) (Supplementary Fig. 7C). The estimated binding affinity (K_d) determined by
339 SSM for Na^+ for NHE9* was 36.3 ± 4 mM and NHE9*CC was 24.1 ± 8 mM, which

340 were similar to the Michaelis–Menten K_M estimate for NHE9* in proteoliposomes
341 (Supplementary Fig. 7D) (Winklemann *et al.*, 2020). Thus, we confirm that we can
342 monitor Na^+ binding to NHE9* using SSM, and that the protein binds sodium ions at a
343 similar concentration range to the *in vivo* K_M estimates measured for other intracellular
344 localized NHE6 and NHE8 isoforms (Pedersen & Counillon, 2019).

345 To assess the influence of PI(3,5)P_2 lipid addition to NHE9* activity, we incubated the
346 purified NHE9* protein with either buffer, or buffer containing solubilised PI(3,5)P_2
347 lipids and reconstituted the respective mixtures into liposomes made from yeast-polar
348 lipids (Methods). SSM-based electrophysiology of NHE9* incubated with buffer
349 produced similar peak currents upon Na^+ addition to those shown previously, whereas
350 NHE9* protein incubated with PI(3,5)P_2 lipid produced a stronger response to Na^+
351 addition (Fig. 5E-F). Consistently, we observed a four-fold increase in its binding
352 affinity for Na^+ (K_d = 9.6 mM) (Fig. 5F). In contrast, PI(4,5)P_2 lipid addition had a
353 similar Na^+ binding affinity as the buffer only samples (Supplementary Fig. 7E). To
354 confirm that the response to PI(3,5)P_2 addition was mediated by the expected interaction
355 with the lysine residues in the TM2-TM3 β-hairpin loop domain, we recorded SSM-
356 based currents for the purified lysine-to-glutamine NHE9* Lys85Gln-Lys105Gln-
357 Lys107Gln variant. The triple glutamine variant also showed a weaker affinity for Na^+
358 (K_d = 55 mM) compared with NHE9* and, in fact, the addition of the PI(3,5)P_2 lipid
359 decreased its apparent affinity for Na^+ (K_d = 88 mM) (Supplementary Fig. 7F). The
360 outside surface of the PI(3,5)P_2-stabilised NHE9* TM2-TM3 β-hairpin loop domain
361 has a partially negatively-charged surface (Fig. 3D). Is seems that stabilization of the
362 TM2-TM3 β-hairpin loop domain by PI(3,5)P_2 lipids provides an electrostatic pathway
363 that can better attract ions to the outward-facing funnel.

364 *Further mechanistic insights from the improved cryo-EM NHE9 CC* structure*
365 In the improved NHE9*CC maps, we were able to confidently model all side-chains
366 forming the ion-binding site, which are positioned around the half-helical cross-over
367 (Fig. 6A and B). We observed some minor differences between the side-chain positions
368 of Thr214, Asp215, Glu239 and Arg408 from the previously reported NHE9* structure
369 (Winklemann *et al.*, 2020), and also between NHE9 and NHE1 (Fig. 5B, C). In MD
370 simulations of NHE9 it was observed that Na^+ can be coordinated within the core
371 domain forming interactions to Asp244, Asn243 Ser240 and Thr214 and several waters

372 (Winklemann *et al.*, 2020). Based on phylogenic analysis (Masrati *et al*, 2018), it was
373 predicted that a salt-bridge would also form between Glu239 in TM6 and Arg408 in
374 TM11. Here, we can confirm a salt-bridge is indeed formed between Glu239 and
375 Arg408 residues and given the position of Glu239 in the ion-binding site, we propose
376 this salt-bridge aids the stabilization of the residues required for coordinating Na^+ (Fig.
377 6C). Moreover, Thr214 forms a parallel hydrogen bond to Asn243 (Fig. 6C). This
378 unexpected hydrogen bond establishes a more rigid ion-binding site than that observed
379 in NHE1, since the Thr214 residue is replaced by valine in NHE1 (Fig. 6B, C). Indeed,
380 all the plasma membrane localized NHE isoforms have a hydrophobic residue in this
381 position, whereas the intracellular isoforms have a threonine residue (Winklemann *et*
382 *al.*, 2020). It's plausible that the structural differences might explain why intracellular
383 isoforms are thought to be able to transport K^+ in addition to Na^+ (Donowitz *et al*, 2013;
384 Pedersen & Counillon, 2019).
385
386 In NHE proteins, extrinsic factors bind to a large, intracellular C-terminal regulatory
387 domain of ~125 – 440 amino acids, which is only found in the mammalian proteins
388 (Brett *et al.*, 2005; Donowitz *et al*, 2009; Fuster & Alexander, 2014; Orlowski &
389 Grinstein, 2004). In NHE1, removal of the regulatory domain results in a
390 constitutionally active transporter (Wakabayashi *et al*, 1992). The C-terminal domain
391 has been referred to as an allosteric regulatory subunit, which influences ion-exchange
392 activity *via* interaction with many effectors (Lacroix *et al*, 2004) e.g., calmodulin
393 (CaM) (Donowitz *et al.*, 2013; Donowitz *et al.*, 2009; Norholm *et al*, 2011; Odunewu-
394 Aderibigbe & Fliegel, 2014; Slepkov *et al*, 2007). The recent human NHE1 structure
395 in complex with Calcineurin B homologous protein 1 (CHP1) revealed an interaction
396 with an interfacial α-helical stretch formed by residues 517 to 539 (Dong *et al.*, 2021).
397 However, CHP1 interacting with the interfacial helix was found to have no direct
398 contacts with the transporter module itself, and is currently unclear how CHP1 binding
399 increases NHE1 activity (Dong *et al.*, 2021). Key to developing an allosteric model for
400 extrinsic regulation is to obtain an NHE structure without complex partners. In the
401 improved NHE9*CC structure, we could model part of the C-terminal domain without
402 protein complex partners (Fig. 6D, Supplementary Fig. 6A). The interfacial helix in the
403 CTD sits on the membrane interface and wraps around from the core domain to the
404 linker helix TM7 (Fig. 6D). In particular, the highly-conserved Lys301 on the linker

405 helix makes direct hydrogen bond interactions to carbonyl of Ile539, backbone amine
406 of Thr541 and carbonyl of Thr541 (Fig. 6D-E and Supplementary Fig. 8). Given that
407 the NHE1 and NHE9 structures superimpose well, apart from the position of the
408 interfacial helix, it seems likely that the binding of CHP1 to the loop region, proceeding
409 the interfacial helix, has driven its dissociation from the linker helix (Fig. 6F,G).
410 Consistently, without CHP1 present, the AlphaFold2 model of NHE1 is similar to
411 NHE9, with clear interactions observed between TM7 and the CTD helix (Fig. 6H).
412 The cytoplasmic surface is also more positively charged with the CTD helix in the likely
413 inhibited position, which could diminish the attraction of positively-charged ions to the
414 inward-facing cavity (Supplementary Fig. 9A-C).

415 **Discussion**

416 Elevator transporters are distinguished from rocker-switch and rocking bundle
417 transporters by the fact that substrates are translocated by just one of the two domains
418 (Drew & Boudker, 2016). The transport domain is able to move independently from the
419 scaffold domain and carry the substrate across the membrane, as the scaffold domain
420 does not participate in substrate binding. It seems in elevator proteins oligomerization
421 is likely required so that the transporter domain can move effectively against the
422 scaffold domain. In some elevator proteins, such as Na^+-coupled glutamate transporters,
423 the scaffold domain is extensive and, once formed, oligomerization is thought to be
424 lipid insensitive. In the Na^+/H^+ exchanger family, however, the scaffold domain can be
425 flexible and shows large structural variations (Winklemann *et al.*, 2020), thus implying
426 a role susceptible to regulation. Indeed, in the Na^+/H^+ exchanger NHA2 (SLC9B2) the
427 additional N-terminal helix can readjust its position in the presence of yeast PI-lipids to
428 make a more compact homodimer (Matsuoka *et al.*, 2022). Moreover, monomeric
429 mutants of NHA2 are inactive and indicate that lipid-remodelling of the homodimer is
430 likely required for functional activity (Matsuoka *et al.*, 2022), although this is yet to be
431 firmly established.

432 Here, we have compared the lipid-mediated oligomerization in the Na^+/H^+ exchanger
433 *E. coli* NhaA and the endosomal exchanger *horse* NHE9, which both harbour β-hairpins
434 located between topologically equivalent helices in the scaffold domain. The scaffold
435 β-hairpin loop domain is absent is bacterial Na^+/H^+ NapA (Lee *et al.*, 2013) and NhaP
436 (Paulino *et al.*, 2014) members, and in mammalian NHEs localised to the plasma

437 membrane (Dong *et al.*, 2021; Dong *et al*, 2022). Moreover, the high structural-
438 similarity between plasma membrane localised NHE1 and endosomal NHE9, implies
439 that the additional TM2-TM3 β-hairpin loop domain has an additional, regulatory role.
440 As expected, CDL binds between NhaA protomers and is stabilised by interaction with
441 arginine residues. In addition, CDL coordination further requires a tryptophan residue
442 located at the end of one of the scaffold helices. Consistently, in computational-based
443 screening for CDL binding to bacterial proteins, a tryptophan residue seems to be a key
444 requirement for ligand lipid-like interactions (Corey *et al.*, 2021). In *horse* NHE9, we
445 observe the PI(3,5)P2 lipid interaction also with a tryptophan residue to one of the
446 scaffolding helices at the dimerization interface. Although positively-charged residues
447 in the TM2-TM3 β-hairpin loop domain are required to stabilise the negatively-charged
448 lipid, the coordination is further established by the tryptophan residue, as well as other
449 polar residues at the dimer interface. In particular, in both structures the lipid interacts
450 with residues in the topologically-equivalent scaffold helices, TM2 in NhaA and TM3
451 in NHE9, which further harbour highly-conserved hydrophobic gating residues
452 (Winklemann *et al.*, 2020). These hydrophobic gating residues are located opposite to
453 the ion-binding site, and they are thought to prevent elevator transitions, unless the
454 negatively-charged aspartate has bound its substrate ion (Winklemann *et al.*, 2020).
455 Thus, we propose a common allosteric coupling between ion-binding and lipid-
456 stabilized oligomerization, whereby stabilization of the scaffold helix enhances Na^+
457 binding. As yet, it is unclear whether catalytic turnover would also increase with
458 scaffold stabilization.

459 The structure of NhaA in complex with CDL supports the proposed regulatory switch
460 induced by salt-stress in *E. coli* (Nji *et al.*, 2018). In NHE9, the specific binding of
461 $PI(3,5)P_2$ is consistent with its subcellular location, and the lipid could either enhance
462 or completely turn on NHE9 activity by stabilizing the homodimer once it reaches late-
463 endosomes (Fig. 7). Consistent with a regulatory switch, $PI(3,5)P_2$ is a minor lipid that
464 is not found in the plasma membrane, but only found in late endosomes and lysosomes
465 (Hasegawa *et al.*, 2017; Ho *et al.*, 2012), which coincides with NHE9 localization.
466 Moreover, the V-type ATPase is known to co-localise with NHE9, and work together to
467 fine-tune organellular pH (Kondapalli *et al.*, 2015). Consistent with the proposed
468 model, the activity of the V-type ATPase is also increased in the presence of $PI(3,5)P_2$
469 lipids (Li *et al*, 2014). Lastly, inhibition of enzymes required to produce $PI(3,5)P_2$ lipids

results in impaired epidermal growth factor receptor (EGFR) trafficking (de Lartigue *et al*, 2009). Indeed, NHE9 activity has been shown to be critical for EGFR sorting and turnover (Kondapalli *et al.*, 2015). Since intracellular NHEs recycle through the plasma membrane they could, in principle, acidify the cell upon exposure to high Na^+ levels, and yet vesicular acidification in NHE7-expressing cells has not been measured (Milosavljevic *et al*, 2014) and NHE9 was likewise found to be inactive at the plasma membrane. To the best of our knowledge, such a lipid-conditioned-activation model would be a novel regulatory mechanism for ion-transporters and SLCs in general.

In addition to the lipid-dependent oligomerization, mammalian NHEs have a long C-terminal regulatory domain that regulates their activity (Pedersen & Counillon, 2019). Bacterial Na^+/H^+ exchangers, like NhaA, lack long C-terminal tails as presumably this level of extrinsic regulation is not required. The C-terminal domain is poorly conserved across the different NHE members and, so far, only part of the C-terminal tail could be modelled for *human* NHE1 in complex with CHP1 (Dong *et al.*, 2021). Structures of human NHE1-CHP1 in outward and inward-facing states show some differences in the position of the C-terminal tail (Dong *et al.*, 2021). Based on these structural differences, it was proposed that CHP1 may increase activity by favouring an outward-facing state. In the improved NHE9*CC structure we could model the corresponding region of the C-terminal tail, but in the absence of any interacting regulatory proteins. Surprisingly, we find that NHE9*CC has a similar interfacial helix between the core and dimer domains to that seen in NHE1. However, in the absence of a regulatory protein, the C-terminal interfacial helix in NHE9*CC is making a number of direct contacts with the linker helix TM7 through interaction with a lysine residue, likely restricting its mobility and that of the core transport domains. An autoinhibitory role of the C-terminal tail has been previously proposed for NHE1 (Wakabayashi *et al*, 1997), which is removed upon Ca^{2+}-calmodulin binding to a site distal to the CTD helix (Sjogaard-Frich *et al*, 2021). Comparing our structure of NHE9 with NHE1-CHP provides a mechanistic framework for the autoinhibitory model, in that the relocation of an auto-inhibitory C-terminal tail by binding partners would remove the brake and enable ion-exchange.

Summary

Our work provides a structural and molecular framework for the allosteric regulation of NhaA and NHE9 Na^+/H^+ exchangers by modulating oligomerization in a specific, lipid-dependent manner. Furthermore, we outline an activation model in the NHEs based on detachment of an CTD helix by accessory factors. Recently, it was shown that plant hormone (auxin) PIN-formed transporters are functional homodimers sharing the same fold as the Na^+/H^+ exchangers (Su *et al*, 2022; Ung *et al*, 2022; Yang *et al*, 2022). PIN transporters likewise harbour a C-terminal regulatory domain of varying length (Krecek *et al*, 2009), and also have both organellar and plasma membrane isoforms (Mravec *et al*, 2009), which must be regulated individually. Moreover, it has been shown that the plasma membrane localized PIN1 is in a dynamic equilibrium between monomers and dimers, and that the dimeric form can be regulated in the plant cell by endogenous flavonols (Teale *et al*, 2021). Thus, the allosteric regulatory mechanisms shown here by lipids and C-terminal tails, could reveal themes relevant to other transporters in general.

Materials and Methods

Expression and purification of NhaA and NHE9* and its variants

Expression and purification of EcNhaA-mut2

*Ec*NhaA WT-like triple mutant (A109T, Q277G, L296M), with a TEV-cleavable C-terminal GFP-His_8 tag was overexpressed in the *E. coli* strain Lemo21 (DE3) and purified as previously described (Lee *et al.*, 2014). Briefly, the *Ec*NhaA triple mutant was extracted from membranes with *n*-Dodecyl β-D-maltoside (DDM; Glycon) and purified by Ni-nitrilotriacetic acid (Ni-NTA; Qiagen) affinity chromatography. To purified NhaA-triple-mutant-GFP fusion, a final concentration of 3 mM cardiolipin (18:1) in 0.05% DDM was added, and then dialyzed overnight against buffer consisting of 20 mM Tris-HCl pH 7.5, 150 mM NaCl and 0.03% DDM. The dialysed *Ec*NhaA-triple-mutant-GFP fusion was subjected to size-exclusion chromatography and the peak concentrated to 3.5 $mg.ml^{-1}$.

534 *Expression and purification of horse NHE9**

535 The *horse* NHE9* structural construct (UniProt accession: F7B133) was identified
536 previously (Winklemann *et al.*, 2020), and is partially truncated on the C-terminal tail
537 consisting of residues 8 to 575 out of a total of 644. The constructs NHE9*CC the
538 L139C-I444C double mutant, NHE9*(N243A-D244A), NHE9*(K85Q-K105Q-
539 K107Q) were synthesized and cloned into the GAL1 inducible TEV-site containing
540 GFP-TwinStrep-His_8 vector $pDDGFP_3$. The cloned *horse* NHE9* and its variants were
541 transformed into the *S. cerevisiae* strain FGY217 and cultivated in 24-L cultures of
542 minus URA media with 0.2% of glucose at 30°C at 150 RPM Tuner shaker flasks using
543 Innova 44R incubators (New Brunswick). Upon reaching an OD_{600} of 0.6 AU galactose
544 was added to a final concentration of 2% (w/v) to induce protein overexpression.
545 Following incubation at the same conditions the cells were harvested 22h after
546 induction by centrifugation (5,000 × *g*, 4°C, 10 min). The cells were resuspended in
547 cell resuspension buffer (CRB, 50 mM Tris-HCl pH 7.6, 1 mM EDTA, 0.6 M sorbitol)
548 and subsequently lysed by mechanical disruption as previously described (Drew *et al*,
549 2008). Centrifugation (10,000 × *g*, 4°C, 10 min) was used to remove cell debris.
550 Membranes were subsequently isolated from the supernatant by ultracentrifugation
551 (195,000 × *g*, 4°C, 2 h), resuspended and homogenized in membrane resuspension
552 buffer (MRB 20 mM Tris-HCl pH 7.5, 0.3 M sucrose, 0.1 mM $CaCl_2$).
553

554 For structural studies of NHE9* at pH 6.5, the membranes were extracted and purified
555 as described previously (Winklemann *et al.*, 2020). In short, the Streptag-purified
556 protein after removal of the C-terminal affinity-GFP-tag was collected and concentrated
557 using 100 kDa MW cut-off spin concentrator (Amicon Merck-Millipore) further
558 purified by size-exclusion chromatography (SEC), using a Superose 6 increase 10/300
559 column (GE Healthcare) and an Agilent LC-1220 system in 20 mM Mes-Tris pH 6.5,
560 150 mM NaCl, 0.003% (w/v) LMNG, 0.0006% (w/v) CHS. For NHE9*CC, the isolated
561 membranes were solubilized as mentioned before (Winklemann *et al.*, 2020) with
562 addition of brain extract from bovine brain type VII (Sigma-Aldrich, cat. nr. B3635) to
563 a total concentration of 0.003mg/ml, in the solublization, wash and elution buffers
564 (Winklemann *et al.*, 2020). The cleaved protein was collected and concentrated using
565 100 kDa MW cut-off spin concentrators (Amicon Merck-Millipore) separated by size-
566 exclusion chromatography (SEC), using a Superose 6 increase 10/300 column (GE

567 Healthcare) and an Agilent LC-1220 system in 20 mM Tris-HCl pH 7.5, 150 mM NaCl,
568 0.003% (w/v) LMNG, 0.0006% (w/v) CHS.

569 **Cryo-EM sample preparation and data acquisition and processing**

570 3 µg of purified NHE9*CC sample was applied to freshly glow-discharged Quantifoil
571 R2/1 Cu300 mesh grids (Electron Microscopy Sciences) and blotted for 3.0s with a 20s
572 waiting time prior, under 100% humidity and subsequently plunge frozen in liquid
573 ethane using a Vitrobot Mark IV (Thermo Fisher Scientific). Cryo-EM datasets were
574 collected on a Titan Krios G3i electron microscope operated at 300 kV equipped with
575 a GIF (Gatan) and a K3 Bioquantum direct electron detector (Gatan) in counting mode.
576 The movie stacks were collected at 130,000× magnification corresponding to a pixel
577 size of 0.66 Å in a counted super-resolution mode. All movies were recorded with a
578 defocus range of -0.4 to -2.5 µm. Similarly, 2.4 µg of purified NHE9* at pH 6.5 was
579 blotted and the movie stacks were collected at 165,000x magnification, with a pixel size
580 of 0.82 Å on Titan Krios G2 electron microscope operated at 300 kV equipped with a
581 GIF (Gatan) and a K2 summit direct electron detector (Gatan) in counting mode The
582 movies were recorded with a defocus range of -0.9 to -2.3 µm. 3µl of *Ec*NhaA-mut2
583 with concentration of 3.5mg/ml was blotted and the movie stack was collected at
584 130,000x magnification, with a pixel size of 0.6645 Å. The movies were recorded with
585 a defocus range of -0.6 to -2.0 µm. The statistics of all cryo-EM data acquisition are
586 summarized in Supplementary Table 1.
587

588 *Image processing NHE9* at pH 6.5:*

589 The dose-fractioned movies were corrected by using MotionCorr2 (Zheng *et al*, 2017).
590 The dose-weighted micrographs were used for contrast-transfer-function estimation by
591 CTFFIND-4.1.13 (Rohou & Grigorieff, 2015). The dose-weighted images were used
592 for auto-picking, classification and 3D reconstruction. Approximately 1,000 particles
593 were manually picked, followed by a round of 2D classification to generate templates
594 for a subsequent round of auto-picking using RELION-3.0 beta (Zivanov *et al*, 2018).
595 The auto-picked particles were subjected to multiple rounds of 2D classification using
596 RELION-3.0 beta to remove bad particles and "junk". The particles belonging to
597 "good" 2D classes were extracted and used for initial model generation using RELION-
598 3.0 beta (Zivanov *et al.*, 2018).

599 To visualize the extracellular loop domain of NHE9, the aligned 244,279 particles from
600 RELION was imported into CryoSPARC (Punjani *et al.*, 2017). *UCSF pyem (Daniel*
601 *Asarnow, 2019)* was used for file format conversion from RELION to CryoSPARC. 3D
602 Variability Analysis (3DVA) in CryoSPARC (Punjani *et al.*, 2017) was performed and
603 set up 6 variable components with the filter resolution 4 Å and high-pass filter 20 Å,
604 respectively. After cluster analysis, the remaining 103,815 particles in 1 of 3 cluster
605 was selected and subsequently, homogeneous refinement in CryoSPARC was
606 performed after applying C2 symmetry and the reconstructed map reached to 3.1 Å
607 resoltuion at the gold standard FSC (0.143).

608 *Image processing NHE9*CC:*
609 The dataset was processed using CryoSPARC (Punjani *et al.*, 2017). Dose fractionated
610 movie frames were aligned using "patch motion correction," and contrast transfer
611 function (CTF) were estimated using "Patch CTF estimation". The particles were
612 picked using automated blob picker. Particles with good 2D classes were used for
613 template based particle picking and extracted using a box size of 300 pixels. 268,054
614 particles were further used for *ab initio* model building and hetero refinements. Final
615 round of non-uniform refinement with C2 symmetry and masked local refinement did
616 result in 3D reconstruction with a gold standard FSC resolution estimation of 3.15Å.
617

618 *Image processing EcNhaA-mut2:*
619 14,329 dose fractionated movie frames were aligned using "patch motion correction,"
620 and contrast transfer function (CTF) were estimated using "Patch CTF estimation" in
621 CryoSPARC (Punjani *et al.*, 2017). 4,401,429 particles were extracted and cleaned up
622 using multiple rounds of 2D classification. 542,404 particles were used for *ab initio*
623 model building and cleaned using multiple rounds of hetero refinement. 78,917
624 particles were further selected for a final round of non-uniform refinement and masked
625 local refinement which resulted in 3D reconstruction with a gold standard FSC
626 resolution estimation of 3.37Å.
627

628 **Cryo EM model building and refinement**
629 Previously determined NHE9 structure (PDB id: 6Z3Z) was fitted into the cryoEM
630 density map of NHE9* CC mutant. Iterative model building and real space refinement
631 was performed using COOT (Emsley *et al*, 2010) and PHENIX.refine (Afonine *et al*,

632 2018). Prior to model building of the extracellular loop domain, AlphaFold2 (AF2) with
633 poly-glycine linker was performed to predict the NHE9 dimer structure assembly. After
634 automatically fitting the initial model into the cryo-EM map, iterative model building
635 and real space refinement was performed using COOT (Emsley *et al.*, 2010) and
636 PHENIX.refine (Afonine *et al.*, 2018). The refinement statistics are summarized in
637 Supplementary Table 1. For generating structural figures PyMOL was used, and for
638 figures of cryo-EM maps either Chimera (Pettersen *et al*, 2004) or ChimeraX (Pettersen
639 *et al*, 2021) was used.
640
641 **All-atom molecular dynamics simulations**
642 The NHE9* CC structure and NHE9* TM2-TM3 loop variant (K58Q, K105Q, K107Q)
643 were embedded into the POPC bilayer and solvated in 0.15 M NaCl using CHARMM-
644 GUI (Qi *et al*, 2015). Either PI(3,5)P_2 and PI(4,5)P_2 were placed in the PIP_2 binding site
645 identified from the cryo-EM structure. All simulations were simulated with a 2 fs
646 timestep using the CHARMM36m forcefield in GROMACS 2022.1(Abraham, 2015).
647 The system was then energy minimised and equilibrated using the standard CHARMM-
648 GUI protocol (Abraham, 2015), where the last step of the protocol was extended to 5
649 ns. The production runs were conducted for 250 ns under 303.15 K using the v-rescale
650 thermostat. The pressure of all systems was maintained at 1 bar using a C-rescale
651 barostat. All simulations were carried out in triplicates, where simulation frames were
652 saved every 0.1 ns.
653
654 **GFP-based thermal shift assay**
655 To characterize lipid binding for NHE9* we used the GFP-Thermal Shift assay
656 (Chatzikyriakidou *et al*, 2021). In brief, purified NHE9*-GFP fusions was isolated as
657 described previously (Winklemann *et al.*, 2020). A buffer containing 20mM Tris,
658 150mM NaCl and 0.03% (w/v) DDM 0.006% (w/v) CHS was used to dilute samples to
659 a final concentration of 0.05–0.075 mg/ml with DDM added to a final concentration of
660 1% (w/v), and incubated for 30 min at 4°C. Stock solutions of the respective lipids,
661 phosphatidylinositol-bis-4,5-phosphate (PI(4,5)P_2 dioctanoyl Echelon Biosciences cat
662 no. P-4508), and phosphatidylinositol-bis-3,5-phosphate (PI(3,5)P_2 dipalmitoyl,
663 Echelon Biosciences cat no. P-3516) were prepared with final concentration of 1 mg/ml
664 in buffer mentioned above. Respective lipids were added to purified NHE9* sample to
665 a final concentration of 0.1 mg/ml and incubated for 10 mins on ice. Subsequently, β-

666 D-Octyl glucoside (Anatrace) was added to a final concentration of 1% (w/v) in 300 µl
667 and the sample aliquots of 100 µl were heated at individual temperatures ranging from
668 20-80°C for 10 min using a PCR thermocycler (Veriti, Applied Biosystems). Heat-
669 denatured material was pelleted at 5000 × g for 30 min at 4°C. The resulting
670 supernatants were collected and fluorescence values recorded (Excitation: 488,
671 Emission 512 nm) using 96-well plate (Thermo Fisher Scientific) measured with
672 Fluoroskan microplate fluorometer (Thermo Scientific) reader. The apparent *T*m was
673 calculated by plotting the average GFP fluorescence intensity from three technical
674 repeats per temperature and fitting a resulting curve using a sigmoidal 4-parameter
675 logistic regression using GraphPad Prism software (GraphPad Software Inc.). The ΔT_M
676 was calculated by subtracting the apparent T_M of the lipid free sample, from the
677 apparent T_M of the sample with the respective lipid added.

678

679 ***Cell-based human NHE1 and NHE9 activity***

680 *Cell culture, constructs and transfection*

681 Cells used for experiments were tested mycoplasma free and grown in a humidified
682 95/5% air/CO2-atmosphere incubator at 37 °C. PS120 fibroblasts, NHE1-null cells
683 derived from Chinese hamster lung fibroblasts CCL39 cells (Pouyssegur *et al*, 1984),
684 were cultured in high glucose DMEM supplemented with 10% fetal bovine serum
685 (FBS), 100 units/mL penicillin and 100 µg/mL streptomycin (reagents from Sigma-
686 Aldrich). Human full length NHE9 was cloned into the pMH vector (Roche) containing
687 a C-terminal HA tag, human full length NHE1 was cloned into p3xFLAG-CMV-14
688 (Sigma-Aldrich) containing a C-terminal 3xFLAG tag. All constructs were verified by
689 sequencing. Transient transfection was performed with Lipofectamine 2000
690 (Invitrogen) according to manufacturer's instructions, and experiments (cell surface
691 expression and transport function studies) were performed 48 hrs after transfection.

692

693 *Cell surface biotinylation*

694 Cell surface biotinylation was performed as described previously (Simonin & Fuster,
695 2010). Cells were rinsed with 1x PBS and surface proteins were biotinylated by
696 incubating cells with 1.5 mg/ml sulfo-NHS-LC-biotin in 10 mm triethanolamine (pH
697 7.4), 1 mm $MgCl_2$, 2 mm $CaCl_2$, and 150 mm NaCl for 90 min with horizontal motion
698 at 4 °C. After labeling, plates were washed with quenching buffer (1xPBS containing 1

699 mm $MgCl_2$, 0.1 mm $CaCl_2$, and 100 mm glycine) for 20 min at 4 °C, then rinsed once
700 with 1xPBS. Cells were then lysed in RIPA buffer (150 mm NaCl, 50 mm Tris·HCl
701 (pH 7.4), 5 mm EDTA, 1% Triton X-100, 0.5% deoxycholate, and 0.1% SDS), and
702 lysates were cleared by centrifugation. Cell lysates of equivalent amounts of protein
703 were equilibrated overnight with streptavidin-agarose beads at 4 °C. Beads were
704 washed sequentially with solutions A (50 mm Tris·HCl (pH 7.4), 100 mm NaCl, and 5
705 mm EDTA) three times, B (50 mm Tris·HCl (pH 7.4) and 500 mm NaCl) two times,
706 and C (50 mm Tris·HCl, pH 7.4) once. Biotinylated proteins were then released by
707 heating to 95 °C with 2.5× Lämmli buffer.
708
709 *SDS-PAGE, immunoblotting and antibodies*
710 SDS-PAGE and immunoblotting were performed as described (Anderegg *et al*, 2020).
711 Cell lysates were separated by SDS-PAGE and transferred to PVDF membranes. The
712 membranes were incubated for 60 minutes with PBS-T20 containing 5% (w/v)
713 skimmed milk. The membranes were then immunoblotted in 5% (w/v) skimmed milk
714 in PBS-T20 with the indicated primary antibodies overnight at 4°C. The blots were then
715 washed three to six times with PBS-T20 and incubated for 1 hour at room temperature
716 with the appropriate secondary HRP-conjugated antibodies in 5% (w/v) skimmed milk
717 in PBS-T20. After repeating the washing steps, the signal was detected with the
718 enhanced chemiluminescence reagent. Immunoblots were developed using a film
719 automatic processor (Fujifilm) and films were scanned with a 600- dpi resolution on a
720 scanner and quantified with ImageJ software. Mouse monoclonal anti-FLAG M2
721 (#F3165), anti-HA (#H9658) and anti-Tubulin (#T9028) antibodies and were obtained
722 from Sigma-Aldrich and used at 1:1000 dilution. HRP-coupled goat anti-mouse IgG
723 antibody (#31430; Invitrogen) was used at 1:2000 dilution, avidin-HRP (#1706528;
724 Bio-Rad) was used at 1:1000 dilution.
725
726 *NHE1 and NHE9 transport activity*
727 NHE activity was measured fluorometrically using the intracellularly trapped pH-
728 sensitive dye BCECF (2′,7′-bis-(Carboxyethyl)-5(6′)-carboxyfluorescein
729 Acetoxymethyl Ester) (#B1170; Invitrogen) with the NH_4Cl prepulse technique as
730 described previously (Simonin & Fuster, 2010). Cells grown on glass coverslips were
731 loaded with 1 μM BCECF-AM and exposed to 25 mM NH_4Cl for 15 min in a buffer

732 containing in mM: 120 NaCl, 5 KCl, 2 $CaCl_2$, 1.5 $MgCl_2$, 25 NH_4Cl, 30 Hepes titrated
733 to pH 7.4 with N-methyl-D-glucamine (NMDG). Then, cells were washed 3x with and
734 incubated in a buffer containing in mM: 120 Tetramethylammonium-Cl (TMACl), 5
735 KCl, 2 $CaCl_2$, 1.5 $MgCl_2$, 30 Hepes titrated to pH 7.4 with NMDG. Recording was
736 started and after 60 s cells were rapidly exposed to a buffer containing in mM: 120
737 NaCl, 5 KCl, 2 $CaCl_2$, 1.5 $MgCl_2$, 30 Hepes titrated to pH 7.4 with NMDG. BCECF
738 fluorescence signals (λ excitation: 490 and 440 nm, λ emission: 535 nm) were recorded
739 in a computer-controlled spectrofluorometer (Fluoromax-2, Photon Technology
740 International). The 490/440 nm fluorescence ratio was calibrated to pHi using the
741 K^+/nigericin method, and initial rate (Vmax; ΔpH/Δtime) of sodium-dependent
742 intracellular pH recovery calculated. (Simonin & Fuster, 2010). All steps of incubation,
743 recording and calibration were performed at 37 °C.
744
745 **Solid Supported Membrane-based electrophysiology**
746 For SSM-based electrophysiology measurements, protein was reconstituted in yeast
747 polar lipids (190001C-100 mg Avanti). The lipids were prepared by solubilization in
748 chloroform and dried using a rotary evaporator (Hei-Vap Core, Heidolph Instruments).
749 Dry yeast polar lipids were thoroughly resuspended in 10 mM MES-Tris pH 8.5,
750 10 mM $MgCl_2$ buffer at a final concentration of 10 mg ml^{-1}. Unilamellar vesicles were
751 prepared by extruding the resuspended lipids using an extruder (Avestin) with 200-nm
752 polycarbonate filters (#10417004 Nuclepore Track-Etch membrane). The vesicles were
753 destabilized by the addition of Na-cholate (0.65% w/v final concentration). SEC-
754 purified protein was added to the destabilized liposomes at a lipid-to-protein ratio
755 (LPR) of 5:1 and incubated for 5 min at room temperature. The sample was added to a
756 PD SpinTrap G-25 desalting column (Cytiva) for removing detergent and the
757 reconstituted proteoliposomes were collected in a final volume of 100µl. The sample
758 was diluted to final lipid concentration of 5 mg ml^{-1} in 10mM MES-Tris pH 7.5, 10 mM
759 $MgCl_2$ buffer, flash frozen in liquid nitrogen and stored at −80 °C until use.
760 Proteoliposomes were diluted 1:1 (vol/vol) with non-activating buffer (10 mM MES-
761 Tris pH 7.5, 300 mM Choline chloride, 10 mM $MgCl_2$) and sonicated using a bath
762 sonicator. 10µl of sample was loaded on 1mm sensor (#161002 Nanion Technologies).
763 For sample measured with $PI(3,5)P_2$, 20µM of the lipid final (v/v) was added to the

764 protein and incubated for 15 min. The sample was subsequently reconstituted in yeast
765 polar lipids as described above.
766
767 Sensor preparation for SSM-based electrophysiology using the SURFE^{2}R N1(Nanion
768 Technologies) system was performed as described previously (Bazzone *et al.*, 2017).
769 During the experiments, NHE9* and NHE9* mutants were activated by solution
770 exchange from non-activating buffer to an activating buffer containing the substrate i.e
771 NaCl. For binding kinetics, *x* mM Choline chloride was replaced by (300 - *x*) mM NaCl
772 in the activating buffer at increasing concentrations. The Na^+-induced peak currents
773 were fitted from triplicate measurements using nonlinear regression curve-fit analysis
774 to a one site specific binding model using GraphPad Prism software. The peak current
775 values were normalized with respect to the average of the maximum value obtained
776 across all measurements. The final K_d values reported are the mean ± s.d. of n = 3
777 independent sensors.

778
779
780
781
782

783 **References**

784 The PyMOL Molecular Graphics System, Version 1.2r3pre ed. Schrödinger, LLC.

785 Abraham MM, T; Roland, S; Páll, S; Smith, J; Hess, B;Lindahl, E (2015) GROMACS:
786 High performance molecular simulations through multi-level parallelism from laptops
787 to supercomputers. *SoftwareX* 1: 19-25

788 Afonine PV, Poon BK, Read RJ, Sobolev OV, Terwilliger TC, Urzhumtsev A, Adams
789 PD (2018) Real-space refinement in PHENIX for cryo-EM and crystallography. *Acta*
790 *Crystallogr D Struct Biol* 74: 531-544

791 Anderegg MA, Albano G, Hanke D, Deisl C, Uehlinger DE, Brandt S, Bhardwaj R,
792 Hediger MA, Fuster DG (2020) The sodium/proton exchanger NHA2 regulates blood
793 pressure through a WNK4-NCC dependent pathway in the kidney. *Kidney Int*

794 Bazzone A, Barthmes M, Fendler K (2017) SSM-Based Electrophysiology for
795 Transporter Research. *Methods Enzymol* 594: 31-83

796 Brett CL, Donowitz M, Rao R (2005) Evolutionary origins of eukaryotic sodium/proton
797 exchangers. *Am J Physiol Cell Physiol* 288: C223-239

798 Chatzikyriakidou Y, Ahn DH, Nji E, Drew D (2021) The GFP thermal shift assay for
799 screening ligand and lipid interactions to solute carrier transporters. *Nat Protoc* 16:
800 5357-5376

801 Coincon M, Uzdavinys P, Nji E, Dotson DL, Winkelmann I, Abdul-Hussein S, Cameron
802 AD, Beckstein O, Drew D (2016) Crystal structures reveal the molecular basis of ion
803 translocation in sodium/proton antiporters. *Nat Struct Mol Biol* 23: 248-255

804 Corey RA, Song W, Duncan AL, Ansell TB, Sansom MSP, Stansfeld PJ (2021)
805 Identification and assessment of cardiolipin interactions with E. coli inner membrane
806 proteins. *Sci Adv* 7

807 Daniel Asarnow EP, & Yifan Cheng. , 2019. UCSF pyem v0.5. Zenodo. p.
808 http://doi.org/10.5281/zenodo.3576630.
809 de Lartigue J, Polson H, Feldman M, Shokat K, Tooze SA, Urbe S, Clague MJ (2009)
810 PIKfyve regulation of endosome-linked pathways. *Traffic* 10: 883-893
811 Dong Y, Gao Y, Ilie A, Kim D, Boucher A, Li B, Zhang XC, Orlowski J, Zhao Y (2021)
812 Structure and mechanism of the human NHE1-CHP1 complex. *Nat Commun* 12: 3474
813 Dong Y, Li H, Ilie A, Gao Y, Boucher A, Zhang XC, Orlowski J, Zhao Y (2022)
814 Structural basis of autoinhibition of the human NHE3-CHP1 complex. *Sci Adv* 8:
815 eabn3925
816 Donowitz M, Ming Tse C, Fuster D (2013) SLC9/NHE gene family, a plasma
817 membrane and organellar family of Na(+)/H(+) exchangers. *Mol Aspects Med* 34: 236-
818 251
819 Donowitz M, Mohan S, Zhu CX, Chen TE, Lin R, Cha B, Zachos NC, Murtazina R,
820 Sarker R, Li X (2009) NHE3 regulatory complexes. *J Exp Biol* 212: 1638-1646
821 Drew D, Boudker O (2016) Shared Molecular Mechanisms of Membrane Transporters.
822 *Annu Rev Biochem* 85: 543-572
823 Drew D, Newstead S, Sonoda Y, Kim H, von Heijne G, Iwata S (2008) GFP-based
824 optimization scheme for the overexpression and purification of eukaryotic membrane
825 proteins in Saccharomyces cerevisiae. *Nat Protoc* 3: 784-798
826 Emsley P, Lohkamp B, Scott WG, Cowtan K (2010) Features and development of Coot.
827 *Acta Crystallogr D Biol Crystallogr* 66: 486-501
828 Fliegel L (2019) Structural and Functional Changes in the Na(+)/H(+) Exchanger
829 Isoform 1, Induced by Erk1/2 Phosphorylation. *Int J Mol Sci* 20
830 Forrest LR (2015) Structural Symmetry in Membrane Proteins. *Annu Rev Biophys* 44:
831 311-337

832 Fuster DG, Alexander RT (2014) Traditional and emerging roles for the SLC9 Na+/H+
833 exchangers. *Pflugers Archiv : European journal of physiology* 466: 61-76
834 Gupta K, Donlan JAC, Hopper JTS, Uzdavinys P, Landreh M, Struwe WB, Drew D,
835 Baldwin AJ, Stansfeld PJ, Robinson CV (2017) The role of interfacial lipids in
836 stabilizing membrane protein oligomers. *Nature* 541: 421-424
837 Hasegawa J, Strunk BS, Weisman LS (2017) PI5P and PI(3,5)P2: Minor, but Essential
838 Phosphoinositides. *Cell Struct Funct* 42: 49-60
839 Hattori M, Hibbs RE, Gouaux E (2012) A fluorescence-detection size-exclusion
840 chromatography-based thermostability assay for membrane protein precrystallization
841 screening. *Structure* 20: 1293-1299
842 Ho CY, Alghamdi TA, Botelho RJ (2012) Phosphatidylinositol-3,5-bisphosphate: no
843 longer the poor PIP2. *Traffic* 13: 1-8
844 Hunte C, Screpanti E, Venturi M, Rimon A, Padan E, Michel H (2005a) Structure of a
845 Na+/H+ antiporter and insights into mechanism of action and regulation by pH. *Nature*
846 435: 1197-1202
847 Hunte C, Screpanti E, Venturi M, Rimon A, Padan E, Michel H (2005b) Structure of a
848 Na+/H+ antiporter and insights into mechanism of action and regulation by pH. *Nature*
849 435: 1197-1202
850 Jumper J, Evans R, Pritzel A, Green T, Figurnov M, Ronneberger O, Tunyasuvunakool
851 K, Bates R, Zidek A, Potapenko A *et al* (2021) Highly accurate protein structure
852 prediction with AlphaFold. *Nature* 596: 583-589
853 Kondapalli KC, Llongueras JP, Capilla-Gonzalez V, Prasad H, Hack A, Smith C,
854 Guerrero-Cazares H, Quinones-Hinojosa A, Rao R (2015) A leak pathway for luminal
855 protons in endosomes drives oncogenic signalling in glioblastoma. *Nat Commun* 6:
856 6289

857 Kondapalli KC, Prasad H, Rao R (2014) An inside job: how endosomal Na(+)/H(+)
858 exchangers link to autism and neurological disease. *Front Cell Neurosci* 8: 172
859 Krecek P, Skupa P, Libus J, Naramoto S, Tejos R, Friml J, Zazimalova E (2009) The
860 PIN-FORMED (PIN) protein family of auxin transporters. *Genome Biol* 10: 249
861 Krulwich TA, Sachs G, Padan E (2011) Molecular aspects of bacterial pH sensing and
862 homeostasis. *Nature reviews Microbiology* 9: 330-343
863 Lacroix J, Poet M, Maehrel C, Counillon L (2004) A mechanism for the activation of
864 the Na/H exchanger NHE-1 by cytoplasmic acidification and mitogens. *EMBO Rep* 5:
865 91-96
866 Landreh M, Marklund EG, Uzdavinys P, Degiacomi MT, Coincon M, Gault J, Gupta
867 K, Liko I, Benesch JL, Drew D *et al* (2017) Integrating mass spectrometry with MD
868 simulations reveals the role of lipids in Na(+)/H(+) antiporters. *Nature communications*
869 8: 13993
870 Lee C, Kang HJ, von Ballmoos C, Newstead S, Uzdavinys P, Dotson DL, Iwata S,
871 Beckstein O, Cameron AD, Drew D (2013) A two-domain elevator mechanism for
872 sodium/proton antiport. *Nature* 501: 573-577
873 Lee C, Yashiro S, Dotson DL, Uzdavinys P, Iwata S, Sansom MS, von Ballmoos C,
874 Beckstein O, Drew D, Cameron AD (2014) Crystal structure of the sodium-proton
875 antiporter NhaA dimer and new mechanistic insights. *The Journal of general*
876 *physiology* 144: 529-544
877 Li SC, Diakov TT, Xu T, Tarsio M, Zhu W, Couoh-Cardel S, Weisman LS, Kane PM
878 (2014) The signaling lipid PI(3,5)P(2) stabilizes V(1)-V(o) sector interactions and
879 activates the V-ATPase. *Mol Biol Cell* 25: 1251-1262

880 Masrati G, Dwivedi M, Rimon A, Gluck-Margolin Y, Kessel A, Ashkenazy H, Mayrose
881 I, Padan E, Ben-Tal N (2018) Broad phylogenetic analysis of cation/proton antiporters
882 reveals transport determinants. *Nat Commun* 9: 4205
883 Matsuoka R, Fudim R, Jung S, Zhang C, Bazzone A, Chatzikyriakidou Y, Robinson
884 CV, Nomura N, Iwata S, Landreh M *et al* (2022) Structure, mechanism and lipid-
885 mediated remodeling of the mammalian Na(+)/H(+) exchanger NHA2. *Nat Struct Mol*
886 *Biol* 29: 108-120
887 Milosavljevic N, Monet M, Lena I, Brau F, Lacas-Gervais S, Feliciangeli S, Counillon
888 L, Poet M (2014) The intracellular Na(+)/H(+) exchanger NHE7 effects a Na(+)-
889 coupled, but not K(+)-coupled proton-loading mechanism in endocytosis. *Cell Rep* 7:
890 689-696
891 Mravec J, Skupa P, Bailly A, Hoyerova K, Krecek P, Bielach A, Petrasek J, Zhang J,
892 Gaykova V, Stierhof YD *et al* (2009) Subcellular homeostasis of phytohormone auxin
893 is mediated by the ER-localized PIN5 transporter. *Nature* 459: 1136-1140
894 Nakamura N, Tanaka S, Teko Y, Mitsui K, Kanazawa H (2005) Four Na+/H+ exchanger
895 isoforms are distributed to Golgi and post-Golgi compartments and are involved in
896 organelle pH regulation. *J Biol Chem* 280: 1561-1572
897 Nji E, Chatzikyriakidou Y, Landreh M, Drew D (2018) An engineered thermal-shift
898 screen reveals specific lipid preferences of eukaryotic and prokaryotic membrane
899 proteins. *Nat Commun* 9: 4253
900 Norholm AB, Hendus-Altenburger R, Bjerre G, Kjaergaard M, Pedersen SF, Kragelund
901 BB (2011) The intracellular distal tail of the Na+/H+ exchanger NHE1 is intrinsically
902 disordered: implications for NHE1 trafficking. *Biochemistry* 50: 3469-3480
903 Odunewu-Aderibigbe A, Fliegel L (2014) The Na(+) /H(+) exchanger and pH
904 regulation in the heart. *IUBMB Life* 66: 679-685

905 Okazaki KI, Wohlert D, Warnau J, Jung H, Yildiz O, Kuhlbrandt W, Hummer G (2019)
906 Mechanism of the electroneutral sodium/proton antiporter PaNhaP from transition-path
907 shooting. *Nat Commun* 10: 1742
908 Orlowski J, Grinstein S (2004) Diversity of the mammalian sodium/proton exchanger
909 SLC9 gene family. *Pflugers Archiv : European journal of physiology* 447: 549-565
910 Padan E (2008) The enlightening encounter between structure and function in the NhaA
911 Na+-H+ antiporter. *Trends Biochem Sci* 33: 435-443
912 Padan E, Tzubery T, Herz K, Kozachkov L, Rimon A, Galili L (2004) NhaA of
913 Escherichia coli, as a model of a pH-regulated Na+/H+antiporter. *Biochimica et*
914 *biophysica acta* 1658: 2-13
915 Paulino C, Wohlert D, Kapotova E, Yildiz O, Kuhlbrandt W (2014) Structure and
916 transport mechanism of the sodium/proton antiporter MjNhaP1. *eLife* 3: e03583
917 Pedersen SF, Counillon L (2019) The SLC9A-C Mammalian Na(+)/H(+) Exchanger
918 Family: Molecules, Mechanisms, and Physiology. *Physiol Rev* 99: 2015-2113
919 Pettersen EF, Goddard TD, Huang CC, Couch GS, Greenblatt DM, Meng EC, Ferrin
920 TE (2004) UCSF Chimera--a visualization system for exploratory research and
921 analysis. *J Comput Chem* 25: 1605-1612
922 Pettersen EF, Goddard TD, Huang CC, Meng EC, Couch GS, Croll TI, Morris JH,
923 Ferrin TE (2021) UCSF ChimeraX: Structure visualization for researchers, educators,
924 and developers. *Protein Sci* 30: 70-82
925 Pouyssegur J, Sardet C, Franchi A, L'Allemain G, Paris S (1984) A specific mutation
926 abolishing Na+/H+ antiport activity in hamster fibroblasts precludes growth at neutral
927 and acidic pH. *Proc Natl Acad Sci U S A* 81: 4833-4837
928 Punjani A, Rubinstein JL, Fleet DJ, Brubaker MA (2017) cryoSPARC: algorithms for
929 rapid unsupervised cryo-EM structure determination. *Nat Methods* 14: 290-296

Qi Y, Ingolfsson HI, Cheng X, Lee J, Marrink SJ, Im W (2015) CHARMM-GUI Martini Maker for Coarse-Grained Simulations with the Martini Force Field. *J Chem Theory Comput* 11: 4486-4494

Quick M, Dwivedi M, Padan E (2021) Insight into the direct interaction of Na(+) with NhaA and mechanistic implications. *Sci Rep* 11: 7045

Rimon A, Mondal R, Friedler A, Padan E (2019) Cardiolipin is an Optimal Phospholipid for the Assembly, Stability, and Proper Functionality of the Dimeric Form of NhaA Na(+)/H(+) Antiporter. *Sci Rep* 9: 17662

Rohou A, Grigorieff N (2015) CTFFIND4: Fast and accurate defocus estimation from electron micrographs. *J Struct Biol* 192: 216-221

Romantsov T, Guan Z, Wood JM (2009) Cardiolipin and the osmotic stress responses of bacteria. *Biochim Biophys Acta* 1788: 2092-2100

Simonin A, Fuster D (2010) Nedd4-1 and beta-arrestin-1 are key regulators of Na+/H+ exchanger 1 ubiquitylation, endocytosis, and function. *J Biol Chem* 285: 38293-38303

Sjogaard-Frich LM, Prestel A, Pedersen ES, Severin M, Kristensen KK, Olsen JG, Kragelund BB, Pedersen SF (2021) Dynamic Na(+)/H(+) exchanger 1 (NHE1) - calmodulin complexes of varying stoichiometry and structure regulate Ca(2+)-dependent NHE1 activation. *eLife* 10

Slepkov ER, Rainey JK, Sykes BD, Fliegel L (2007) Structural and functional analysis of the Na+/H+ exchanger. *Biochem J* 401: 623-633

Su N, Zhu A, Tao X, Ding ZJ, Chang S, Ye F, Zhang Y, Zhao C, Chen Q, Wang J *et al* (2022) Structures and mechanisms of the Arabidopsis auxin transporter PIN3. *Nature*

Suades A, Qureshi A, McComas SE, Coincon M, Rudling A, Chatzikyriakidou Y, Landreh M, Carlsson J, Drew D (2023) Establishing mammalian GLUT kinetics and lipid composition influences in a reconstituted-liposome system. *Nat Commun* 14: 4070

Teale WD, Pasternak T, Dal Bosco C, Dovzhenko A, Kratzat K, Bildl W, Schworer M, Falk T, Ruperti B, Schaefer JV *et al* (2021) Flavonol-mediated stabilization of PIN efflux complexes regulates polar auxin transport. *The EMBO journal* 40: e104416

Ung KL, Winkler M, Schulz L, Kolb M, Janacek DP, Dedic E, Stokes DL, Hammes UZ, Pedersen BP (2022) Structures and mechanism of the plant PIN-FORMED auxin transporter. *Nature*

Wakabayashi S, Fafournoux P, Sardet C, Pouyssegur J (1992) The Na+/H+ antiporter cytoplasmic domain mediates growth factor signals and controls "H(+)-sensing". *Proc Natl Acad Sci U S A* 89: 2424-2428

Wakabayashi S, Ikeda T, Iwamoto T, Pouyssegur J, Shigekawa M (1997) Calmodulin-binding autoinhibitory domain controls "pH-sensing" in the Na+/H+ exchanger NHE1 through sequence-specific interaction. *Biochemistry* 36: 12854-12861

Winkelmann I, Uzdavinys P, Kenney IM, Brock J, Meier PF, Wagner LM, Gabriel F, Jung S, Matsuoka R, von Ballmoos C *et al* (2022) Crystal structure of the Na(+)/H(+) antiporter NhaA at active pH reveals the mechanistic basis for pH sensing. *Nat Commun* 13: 6383

Winklemann I, Matsuoka R, Meier PF, Shutin D, Zhang C, Orellana L, Sexton R, Landreh M, Robinson CV, Beckstein O *et al* (2020) Structure and elevator mechanism of the mammalian sodium/proton exchanger NHE9. *The EMBO journal* 39: e105908

Wohlert D, Kuhlbrandt W, Yildiz O (2014) Structure and substrate ion binding in the sodium/proton antiporter PaNhaP. *eLife* 3: e03579

Yang Z, Xia J, Hong J, Zhang C, Wei H, Ying W, Sun C, Sun L, Mao Y, Gao Y *et al* (2022) Structural insights into auxin recognition and efflux by Arabidopsis PIN1. *Nature*

Yeo H, Mehta V, Gulati A, Drew D (2023) Structure and electromechanical coupling of a voltage-gated Na(+)/H(+) exchanger. *Nature* 623: 193-201

Zhang-James Y, Vaudel M, Mjaavatten O, Berven FS, Haavik J, Faraone SV (2019) Effect of disease-associated SLC9A9 mutations on protein-protein interaction networks: implications for molecular mechanisms for ADHD and autism. *Atten Defic Hyperact Disord* 11: 91-105

Zheng SQ, Palovcak E, Armache JP, Verba KA, Cheng Y, Agard DA (2017) MotionCor2: anisotropic correction of beam-induced motion for improved cryo-electron microscopy. *Nat Methods* 14: 331-332

Zivanov J, Nakane T, Forsberg BO, Kimanius D, Hagen WJ, Lindahl E, Scheres SH (2018) New tools for automated high-resolution cryo-EM structure determination in RELION-3. *eLife* 7

992 **Acknowledgements**

993 We are grateful to Marta Carroni at the Cryo-EM Swedish National Facility at SciLife
994 Stockholm for cryo-EM data collection as well as Michael Hall at the Umeå Core
995 Facility for Electron Microscopy, UCEM and the European Synchrotron Radiation
996 Facility (ESRF). The computations were enabled by resources provided by the Swedish
997 National Infrastructure for Computing (SNIC) at the PDC Center for High Performance
998 Computing, KTH Royal Institute of Technology, partially funded by the Swedish
999 Research Council through grant agreement no. 2018-05973. This work was funded a
1000 European Research Council (ERC) Consolidator Grant EXCHANGE (Grant no. ERC-
1001 CoG-820187) to D.D

1002 **Author contributions**

1003 D.D. designed the project. Cloning, expression screening and sample preparation for
1004 cryo-EM was carried out by P.M. and S.K. Cryo-EM data collection and map
1005 reconstruction was carried out by P.M, S.K, R.M, A.G an D.D. Model building was
1006 carried out by R.M, A.G and D.D. MD simulations were carried out by T.D and L.D.
1007 All authors discussed the results and commented on the manuscript. The authors declare
1008 no competing financial interests. Correspondence and request for materials should be
1009 addressed to D.D. (d.drew@dbb.su.se).

1010 **Data availability**

1011 The coordinates and the maps for cryo-EM structures of *horse* NHE9* with TM2-TM3
1012 loop at pH 6.5, *hor*se NHE9* CC bound to PI(3,5)P_2, and the *E. coli* NhaA dimer with
1013 cardiolipin, have been deposited in the Protein Data Bank (PDB) and Electron
1014 Microscopy Data Bank (EMD) with entries PDB ID: 8PVR, 8PXB, 8PS0, respectively.

1015

1016

1017

Fig. 1

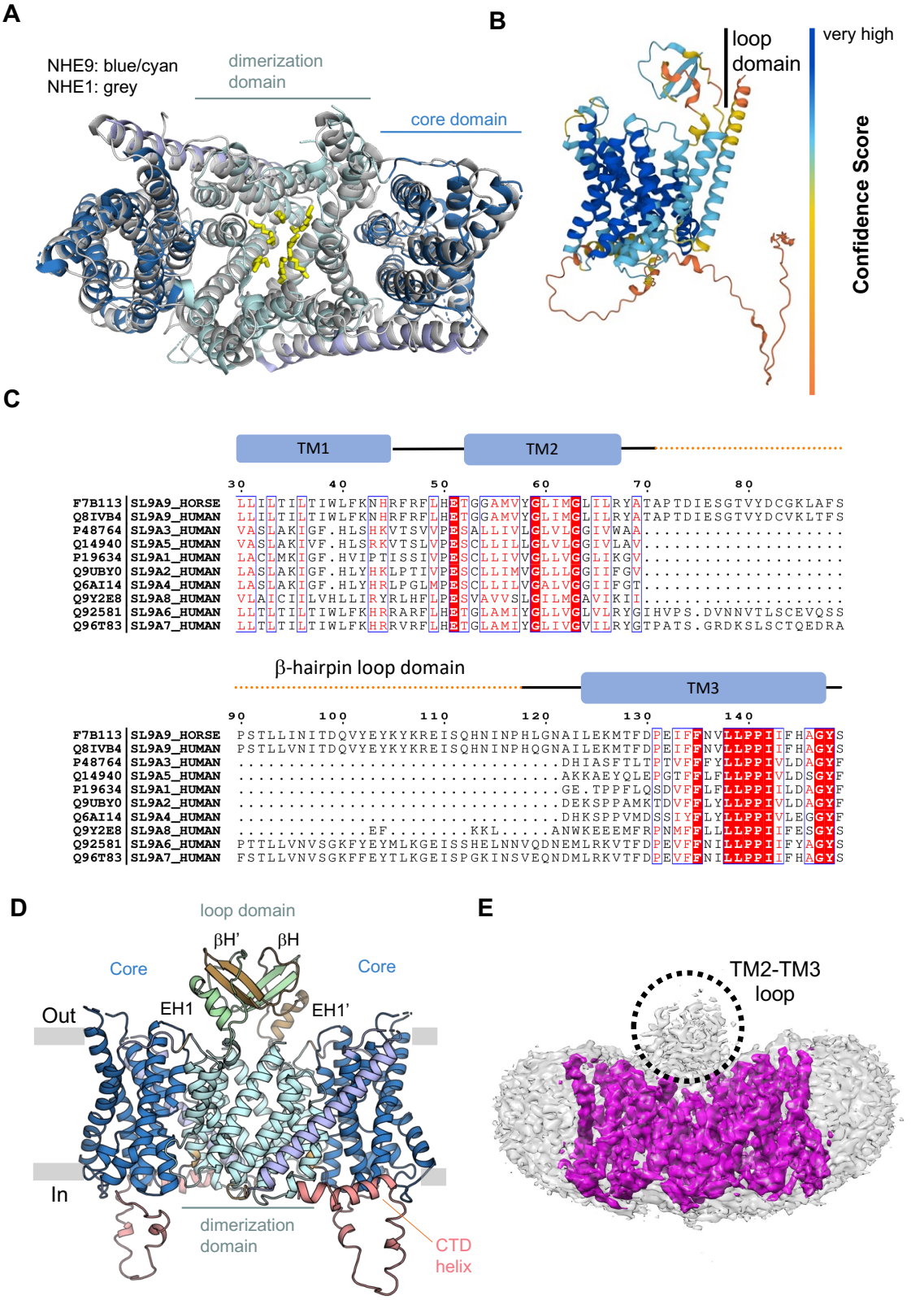

1018 **Figure 1. AlphaFold2 model for endosomal NHE9 includes β-hairpin TM2-TM3**

1019 **loop domain**. (**A**) Structural superimposition of *horse* NHE9* with inward-facing

NHE1 (C_α RMSD = 2.91 Å) shows the overall structural conservation. Inward-facing NHE9 ΔCTD (PDB: 6Z3Z) with dimerization domain (cyan), core domain (blue) and TM7 linking helix (light-purple) all shown as cartoon. Inward-facing NHE1 (PDB: 7DSW) (grey, cartoon) with its lipids (yellow, sticks) inside the cavity between the dimerization domains. (**B**) AF2 model of the *human* NHE9 monomer that predicts an additional TM2-TM3 loop domain containing a β-hairpin with reasonable confidence. **(C)** The *human* NHE1-9 sequence alignment for TM1 to TM3. Residues with over 90% sequence identity are shown in red. The β-hairpin TM2-TM3 loop is only present in organellular NHE6, NHE7 and NHE9 proteins. (**D**). AF2 model of the *horse* NHE9 dimer with an TM2-TM3 loop domain containing an β-hairpin (βH1, βH1') and extracellular helix (EH1, EH1') from each of the two protomers coloured in brown and green, respectively. The core domain (dark-blue), dimerization domain (light-blue) and CTD domain (salmon) is further highlighted. (**E**) NHE9* structure and maps (PDB: 6Z3Z, EMD: EMD-11067) at low contour levels to highlight the loop domain map features that could not be modelled (black-dotted circle).

Fig. 2

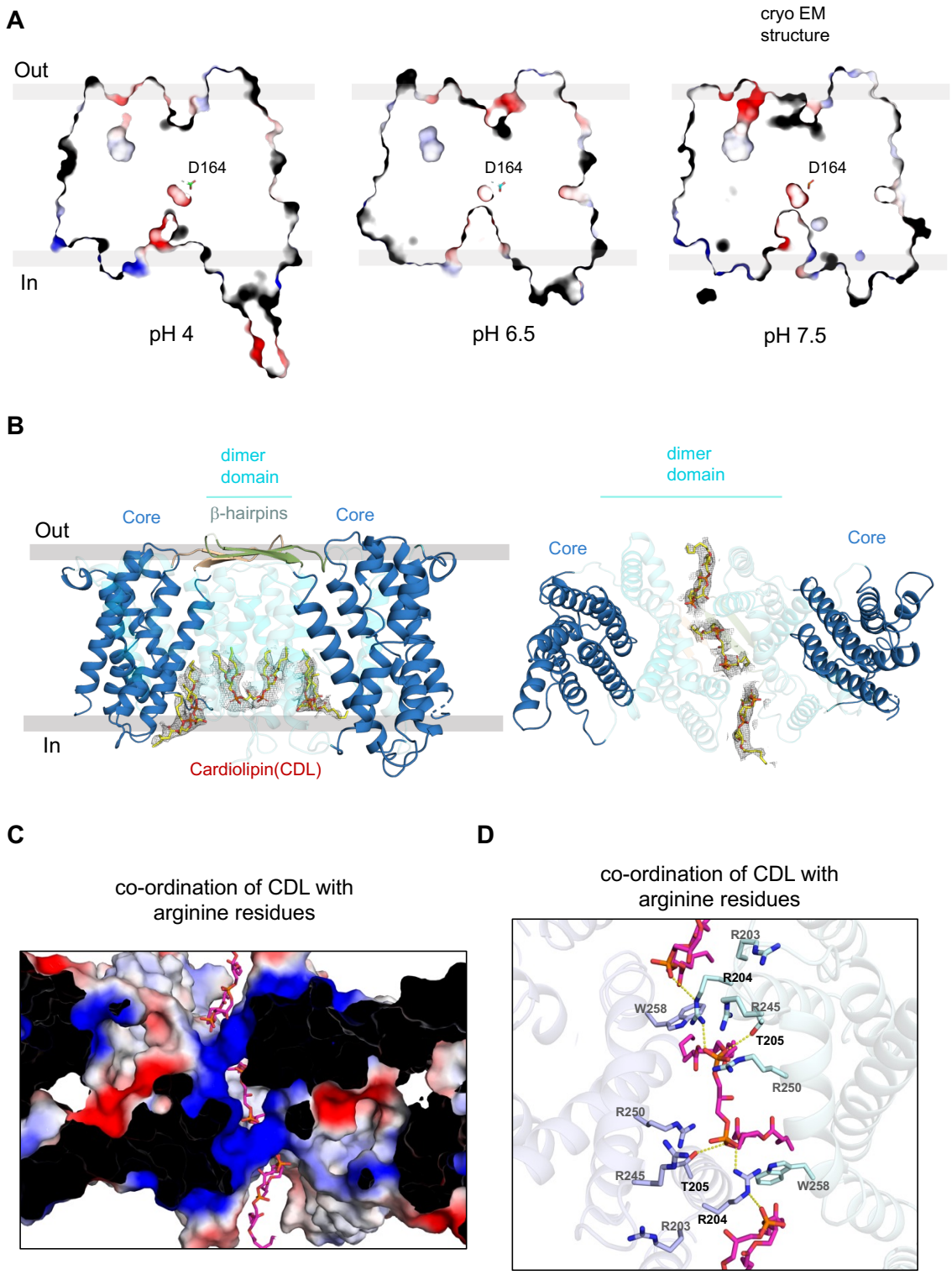

1046

1047 **Figure 2. Structure of cardiolipin (CDL) bound to *Ec*NhaA homodimer.** (**A**) Slice
1048 through an electrostatic surface representation of *Ec*NhaA structures, perpendicular to
1049 the membrane plane, at active pH 6.5 (left, PDB ID: 7S24), inactive pH 4.0 (right, PDB

1050 ID: 4AU5) and pH 7.5-CDL bound. The ion-binding aspartate is indicated and shown
1051 as cyan sticks. The ion-binding funnel at the cytoplasmic side is much more open at
1052 active pH 6.5 and pH 7.5-CDL bound structure than at pH 4. (**B**) *left:* Model of *Ec*NhaA
1053 homodimer obtained by cryo-EM and with β-hairpin loop domains (palegreen, sand,
1054 cartoon). Large densities between the dimerization domains indicate the presence of
1055 three CDL (yellow, sticks) fitted in the model. *right* Cytoplasmic view of *Ec*NhaA
1056 model with the three CDL fitted between the dimer domains. (**C**) Cytoplasmic view of
1057 slice through an electrostatic surface potential map with three cardiolipins (mangenta,
1058 sticks) positioned in the hydrophobic and positively-charged dimerization interface
1059 (blue). (**D**) Cytoplasmic view of *Ec*NhaA model (cartoon) with CDL (magenta, sticks)
1060 coordinating residues. Positively charged arginine residues are labelled and shown in
1061 cyan and purple sticks.

1062

1063

1064

1065

1066

1067

1068

1069

1070

1071

1072

1073

1074

1075

1076

Fig. 3

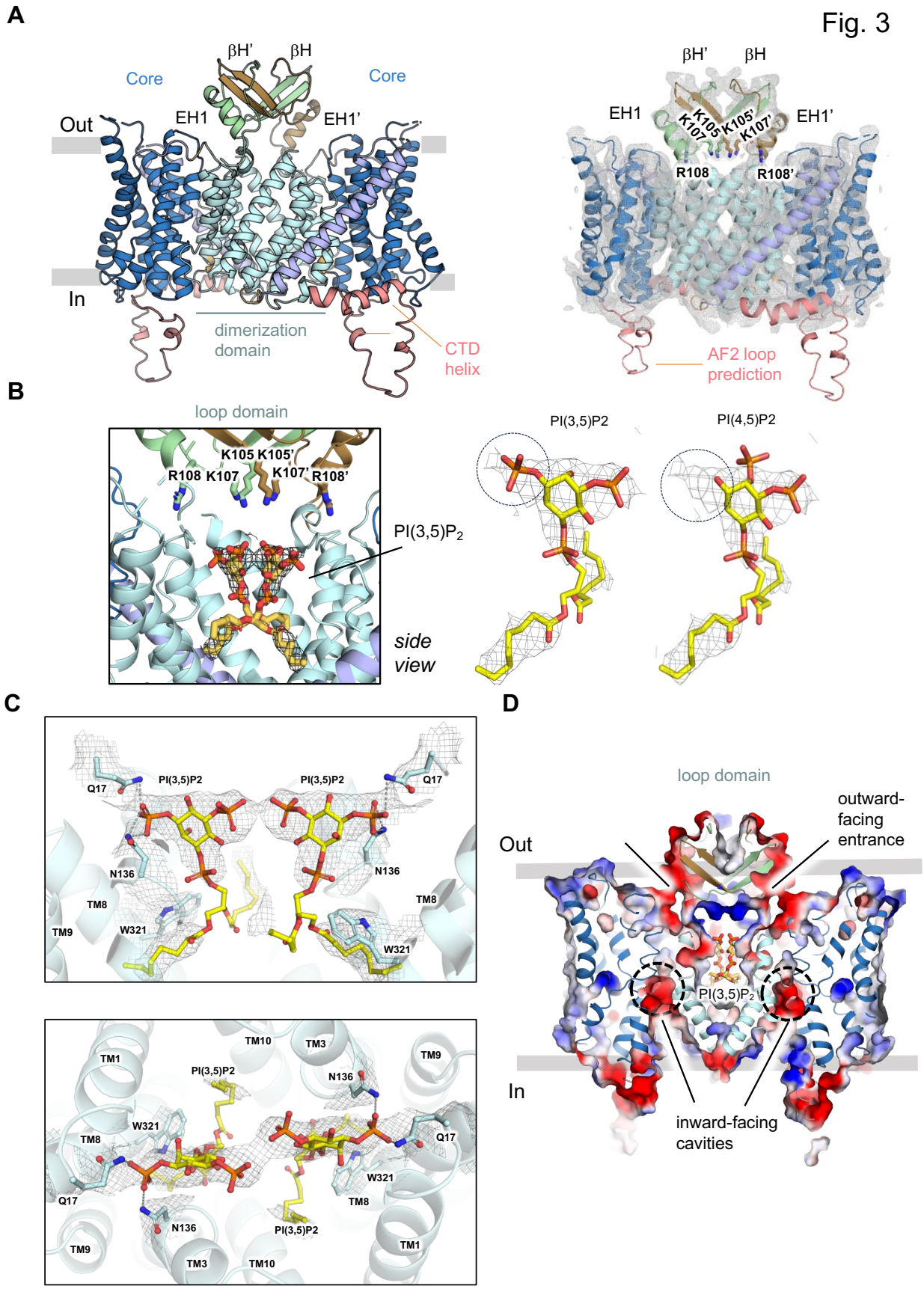

1077

1078 **Figure 3. TM2-TM3 β-loop domain structure of NHE9* CC with negatively-**
1079 **charged PI(3,5)P_2 lipids bound at the dimer interface. (A)** *left:* Structure of the *horse*
1080 NHE9* structure determined by cryo-EM and guided by the refined NHE9* model for
1081 the β-hairpin TM2-TM3 loop domain. Domain-swapped βH, βH' and EH1, EH1' in
1082 green and brown respectively, and NHE9 core and dimer domains coloured as in Fig.
1083 1D. An additional C-terminal helix in the CTD could be modelled (salmon, cartoon),
1084 but there is no density to support the 20 residue AF2 loop model that is located between
1085 the end of the core domain and the beginning of the interfacial helix *right:* The cryo
1086 EM maps for the *horse* NHE9* structure including the charged residues in loop domain
1087 highlighted in sticks. **(B)** *left:* In the *horse* NHE9* CC structure additional map density
1088 supported the modelling of two PIP_2 lipids (yellow sticks) located in the middle at the
1089 dimerization interface between the two protomers and could interact with the positively
1090 charged β-hairpin TM2-TM3 loop domain residues (green and brown sticks). *right:* The
1091 fitting of PI(3,5)P_2 vs PI(4,5)P_2 lipids into the cryo EM maps are compared. (**C**) In
1092 addition to the β-hairpin TM2-TM3 loop domain lysine residues, PI(3,5)P2 is
1093 coordinated at the dimerization interface by aromatic and polar residues Trp321, Gln17,
1094 Asn136. TM segments TM1 and TM8 are not shown for better visualization of the
1095 bound lipids (yellow sticks and grey mesh) **(D)** Electrostatic surface potential map
1096 cross-section with two negatively-charged PI(3,5)P_2 modelled in the hydrophobic and
1097 positively-charged dimerization interface (blue). The interface between the loop
1098 domains and core domains (indicated by the black-line) are negatively-charged and
1099 provide an electrostatic pathway for cations in the outward-facing state. Protein shown
1100 as cartoon colored as in Fig. 1E, and PI(3,5)P_2 as yellow-sticks and the ion-binding site
1101 is highlighted (dotted-circle).

1102

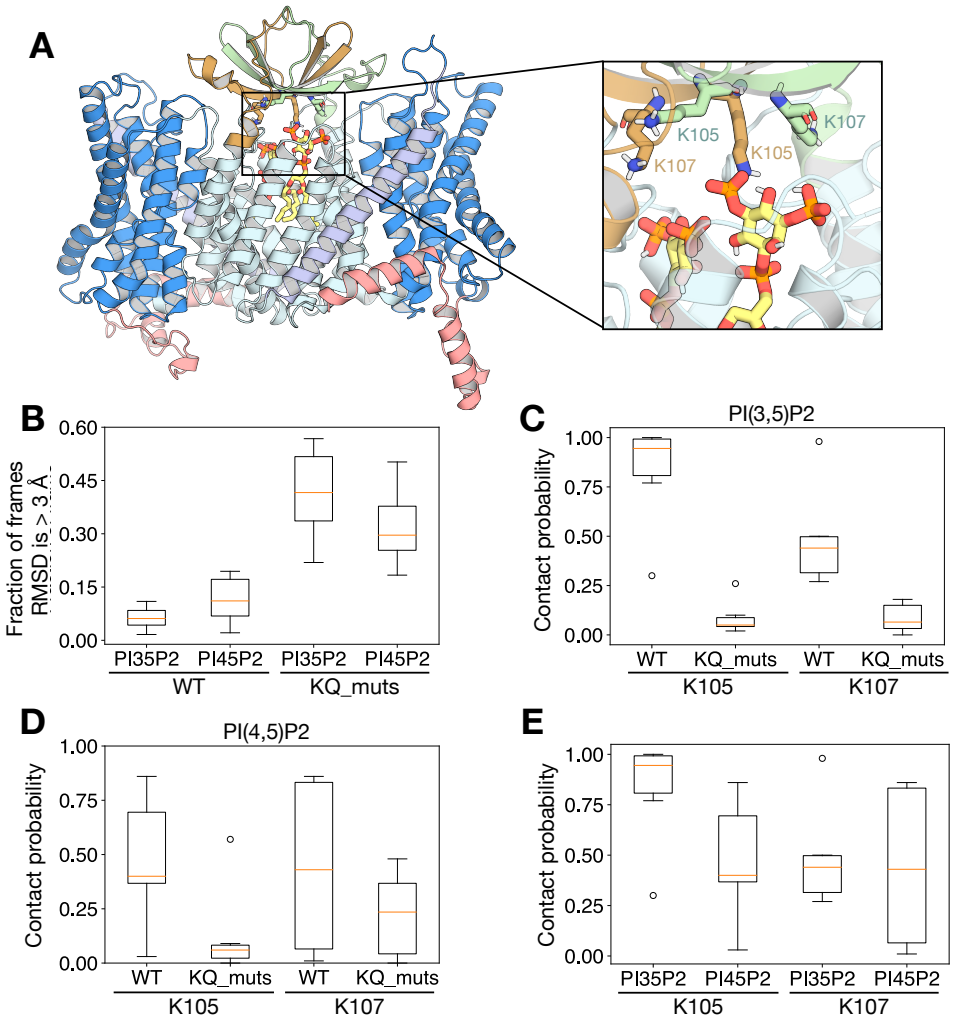

Figure 4. MD simulations of PIP_2 interaction to NHE9* CC. (**A**) A representative snapshot of NHE9 with $PI(3,5)P_2$ after a 250 ns simulation. The structure of $PI(3,5)P_2$ is shown in yellow. K105 and K107 of the different protomers are shown in green and brown, respectively. Protein shown as cartoon and lipids as sticks (colored as in Fig. 1D). (**B**) Box plot representation of the distribution of the fractions of frames where the root mean square deviation (RMSD) of PIP_2 lipids is > 3 Å with respect to its previous 10 ns structure. (**C**) Box plot representation of the distribution of frames where $PI(3,5)P_2$ are within 4 Å (defined as contact probability) with either K105, K107 or its mutants. (**D**) Box plot representation of the distribution of frames where $PI(4,5)P_2$ are within 4 Å (defined as contact probability) with either K105, K107 or its mutants. (**E**) Box plot representation of the distribution of the contact probability between K105 and K107 with either $PI(3,5)P_2$ or $PI(4,5)P_2$.

1115

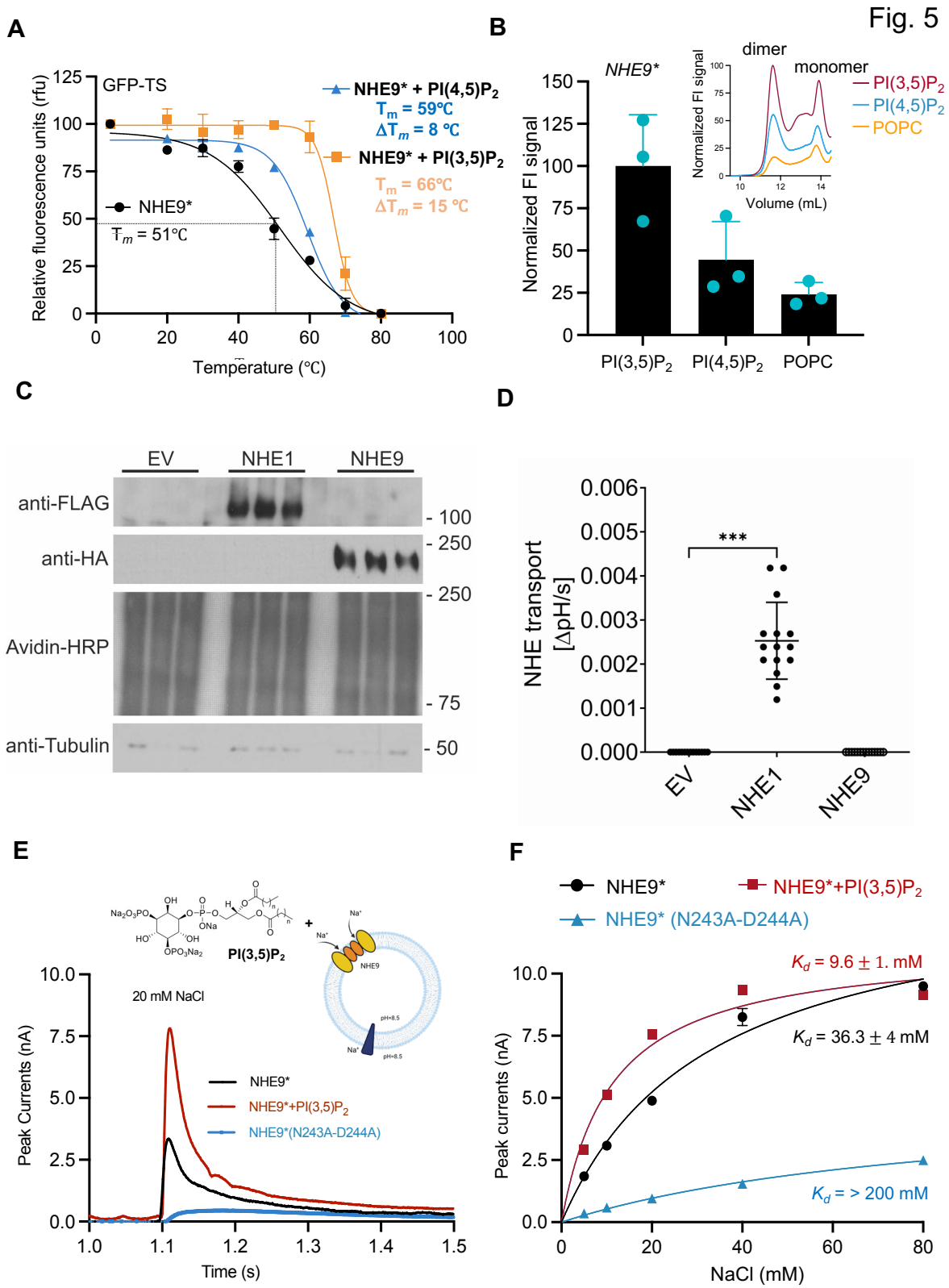

1116

1117 **Figure 5. NHE9 is non-functional at the plasma membrane and the endosomal-**
1118 **specific lipid PI(3,5)P$_2$ stabilizes the functional homodimer and activity. (A)**

1119 Thermal shift stabilization of purified dimeric NHE9*-GFP in the presence of PI(4,5)P_2
1120 (blue) and PI(3,5)P_2 (mustard) compared to lipid-free (black). Data presented are
1121 normalized fluorescence of mean values ± data range of n = 3 technical repeats; the
1122 apparent T_M was calculated from datapoints fitted according to a sigmoidal 4-parameter
1123 logistic regression function. (**B**) Bars represent the normalised fraction of NHE9*
1124 homodimer remaining after heating at 50ºC for 10 mins in the presence of DDM-
1125 solublised lipids as labelled, which was asseded by FSEC. Error bars are the SEM of
1126 n = 3 FSEC injections, *top inset:* representative FSEC traces of the tabulated data
1127 shown. (**C**) Plasma membrane expression of FLAG-tagged NHE1 and HA-tagged
1128 NHE9 in PS120 cells. PS120 were transfected with empty vector (EV; pMH), human
1129 NHE1 or human NHE9. Plasma membrane proteins were isolated using surface
1130 biotinlyation. Avidin–HRP was used as loading control. The absence of a strong tubulin
1131 signal confirms the purity of the membrane fraction. Three independent biological
1132 replicates per condition. (**D**) NHE transport activity in transfected PS120 cells.
1133 Measurement of plasma membrane NHE transport activity in empty vector (EV;
1134 negative control), human NHE1 (positive control) or human NHE9 transfected PS120
1135 cells by quantification of the sodium-dependent intracellular pH recovery after
1136 acidification of the cytoplasm. Values are shown as means ±SD. (**E**) SSM-based
1137 electrophysiology. Transient currents were recorded for NHE9* proteoliposomes (black
1138 trace) at symmetrical pH 7.5 after the addition of 20 mM NaCl. Peak currents for an
1139 ion-binding site NHE9* variant N243A-D244A (blue trace) and NHE9* pre-incubated
1140 with synthetic PI(3,5)P_2 lipids (red trace) are also shown. *above:* schematic of NHE9*
1141 and PI(3,5)P_2 reconstituted into liposomes for SSM based electrophysiology
1142 measurements (**F**) Fit of the amplitude of the transient currents as a function of Na^+
1143 concentrations at pH 7.5 for horse NHE9* proteoliposomes pre-incubated with either
1144 buffer (black-trace) or synthetic PI(3,5)P_2 lipids (red trace) and the corresponding
1145 binding affinity (K_D). Error bars are the mean values ± s.e.m. of: n = 3 individual
1146 repeats.

1147

1148

1149

1150

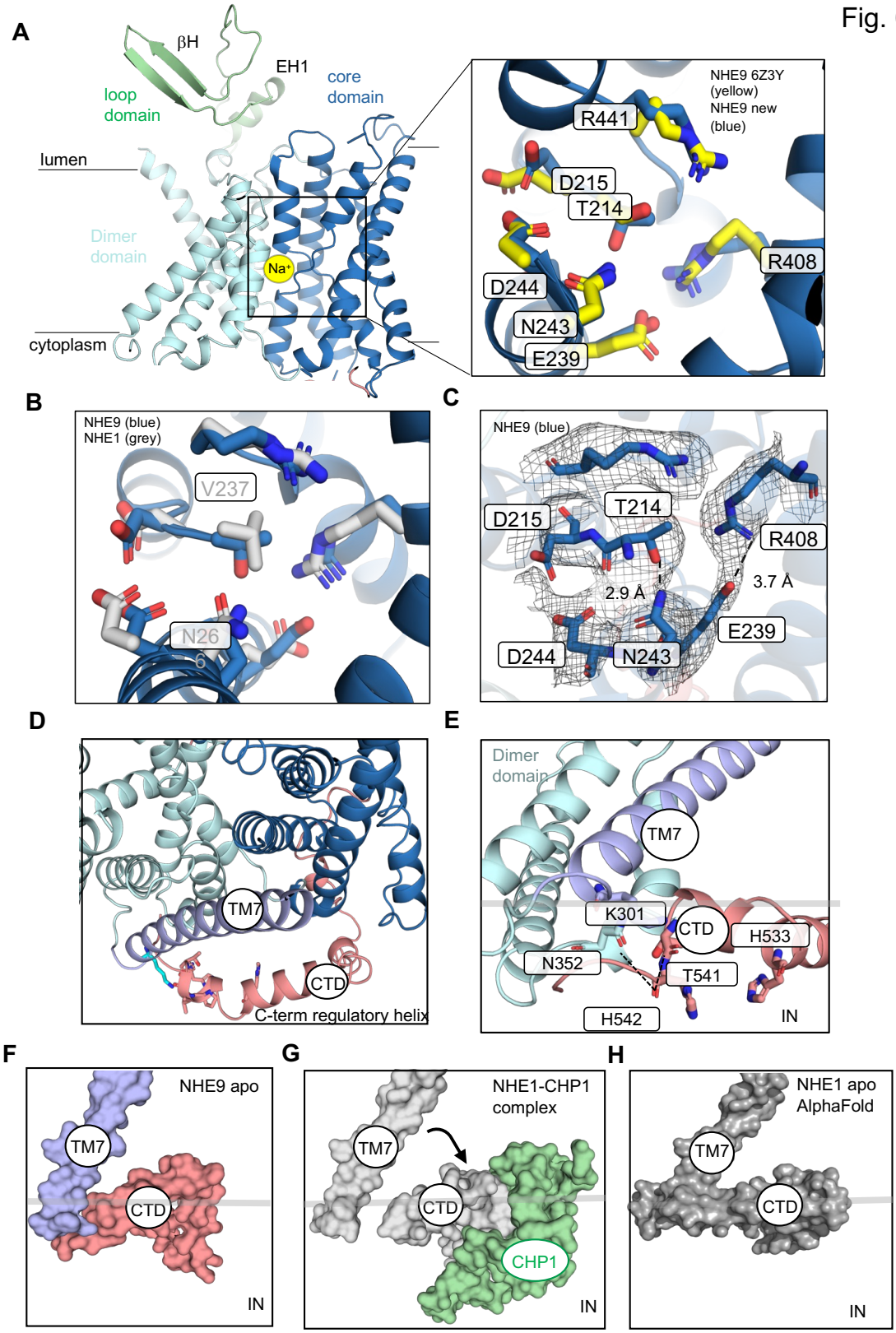

1151

1152 **Figure 6. Ion-binding site and C-terminal domain of the NHE9*CC (A)** *left:*
1153 cartoon representation of the NHE9 ion-binding site, located in the 6-TM core
1154 transporter domain, which is made up of two broken helices. The sodium ion (yellow

sphere) is located and coordinated at the ion-binding site. *right:* ion-binding residues of the NHE9*CC structure are shown as blue sticks and labelled, with the identical residues of NHE9* shown as yellow sticks (PDB id: 6Z3Y). **(B)** Ion-binding residues of NHE9*CC are shown as blue sticks and NHE1 residues shown as grey sticks with Val237 labelled**. (C)** Hydrogen-bonding between T214-N243 and salt-bridge interaction between E239-R408 in the NHE9*CC structure are illustrated by dashed lines and the cryo EM maps shown as grey mesh. (**D**) Top view showing how the CTD helix is positioned on the outside of the mobile TM7 linker domain. (**E**) Numerous contacts are formed between the CTD and the linker helix TM7 and in particular K301 (blue-sticks) in TM7 and the CTD helix (salmon sticks) and labelled. **(F)** In the horse NHE9* CC structure the CTD stays connected to the linker helix TM7 (protein shown as surface). **(G)** CHP1 (green, surface) binding to the CTD of NHE1 (grey, surface) moves it away from the linker helix TM7. (**H)** AF2 model of NHE1 predicts CTD interacts to TM7 as seen in the NHE9* CC cryo EM structure.

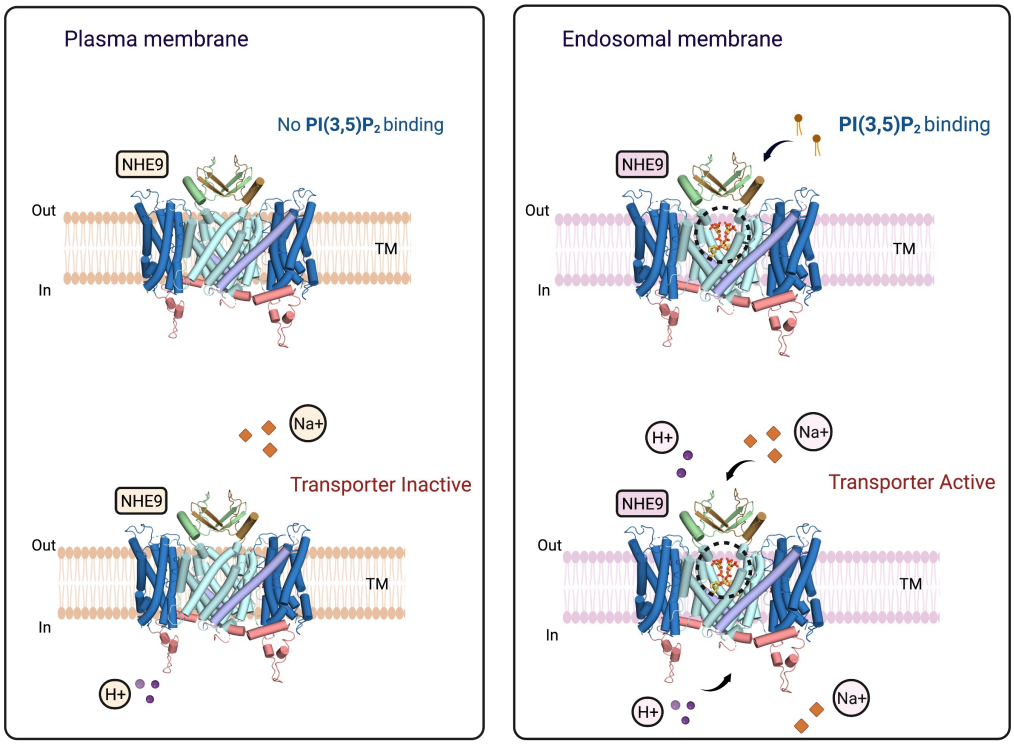

1171

1172 **Figure 7. The PI(3,5)P_2-dependent activation of NHE9 in late endosomes.**
1173 Schematic representation of NHE9 ion translocation, dimer stabilisation and transport
1174 activation in the endosomes vs. the cell membrane. NHE9 is inactive in the plasma
1175 membrane. Upon relocation into late endosomes, a concomitant binding of PI(3,5)P_2 at
1176 the dimerization interface improves the stability of homodimer and activates the
1177 transporter. The figure was created using Biorender.com

1178